AGU100 ADVANCING EARTH AND SPACE SCIENCE

JGR

Journal of Geophysical Research: Atmospheres

RESEARCH ARTICLE

10.1029/2017JD028114

The Influence of Real-World Wind Turbine Deployments on Local to Mesoscale Climate

S. C. Pryor[1], R. J. Barthelmie[2], and T. J. Shepherd[1]

[1]Department of Earth and Atmospheric Sciences, Cornell University, Ithaca, NY, USA, [2]Sibley School of Mechanical and Aerospace Engineering, Cornell University, Ithaca, NY, USA

Key Points:
- High-resolution numerical simulations of the effects of wind turbines on local to mesoscale climate indicate modest impacts
- Previous research may have inadvertently overestimated the effects of current wind turbines on local-to-mesoscale climates
- Impacts on temperature, specific humidity, precipitation, and sensible and latent heat fluxes are statistically significant only in summer

Correspondence to:
S. C. Pryor,
sp2279@cornell.edu

Citation:
Pryor, S. C., Barthelmie, R. J., & Shepherd, T. J. (2018). The influence of real-world wind turbine deployments on local to mesoscale climate. *Journal of Geophysical Research: Atmospheres*, *123*, 5804–5826. https://doi.org/10.1029/2017JD028114

Received 24 NOV 2017
Accepted 5 MAY 2018
Accepted article online 15 MAY 2018
Published online 4 JUN 2018

Abstract Paired simulations are conducted using the Weather Research and Forecasting model applied at convection permitting resolution in order to determine the impact of wind turbines (WTs) on the local to mesoscale climate. Using actual WT locations and a model of the effect of the WT rotor on the flow field, it is shown that while the presence of WT changes wind speeds (WSs) and near-surface air temperature in 4-km grid cells in which WTs are located, the impact at larger scales on near-surface air temperature, specific humidity, the fluxes of latent and sensible heat, boundary layer heights, and precipitation is not significant in any season other than summer. During summer, the maximum pairwise difference in grid cell mean temperatures is 0.5 K and the maximum increase in near-surface specific humidity is 0.4 g/kg. However, a spatial average of the mean seasonal perturbation of air temperature by WT gives a net impact of <0.1 K. Precipitation probability is also not significantly impacted in any season other than summer. In the summer the presence of WT is associated with a small decrease in precipitation probability and a decrease in season total precipitation of -2.6%. The finding of minor magnitude, but significant impacts, during summer should be used to contextualize results of substantial climate impacts from WT arrays deployed in the U.S. Central Plains based on short-term simulations conducted for the summer season.

Plain Language Summary Decarbonizing the electricity supply via increased use of renewable energy sources has been proposed as an effective climate change mitigation strategy, but concerns have been raised that large-scale deployments of wind turbines may alter local to regional climate. Using simulations conducted for climatologically relevant time periods and realistic representations of both the locations of wind turbines and their interaction with the atmosphere, we show that for current deployments this impact is negligible.

1. Introduction and Objectives

Decarbonizing the global energy supply via expanded use of renewable energy systems including wind turbines (WTs), is an integral component of efforts to transition the energy system to provide sustainable and secure supply of electricity while reducing undesirable environmental impacts (Barthelmie & Pryor, 2014; Edenhofer et al., 2012; National Renewable Energy Laboratory, 2008). Electricity from WT currently supplies 4.3% and 6% of the global and U.S. national supply, respectively (Wiser et al., 2016; Wiser & Bolinger, 2016), and is projected to exceed 20% of U.S. electricity consumption by 2030 (National Renewable Energy Laboratory, 2008). Achieving this target would require an approximate quadrupling of installed wind energy capacity (from the current value of 84 GW [July 2017]). However, although onshore WT deployments are cost-competitive electricity generation sources (Wiser & Bolinger, 2017), questions remain about possible impacts of harnessing "the power of the wind" on the local to regional environment (i.e., "inadvertent weather/climate modification").

WT extract momentum from the atmosphere and convert it into electrical power. The action of doing so leads to a decrease in WSs behind the rotor plane along with increases in turbulent kinetic energy (TKE) and vertical exchange. WT wakes (the volume of air with decreased WSs and increased turbulent motions behind a turbine rotor) have been extensively studied in the context of determining the role of atmospheric conditions on their behavior and in terms of optimizing electrical power yield from WTs by optimizing WT arrays (e.g., Barthelmie et al., 2013; Frandsen et al., 2009; Prospathopoulos et al., 2011). These near-field impacts on flow regimes are unavoidable and thus some impact on the local thermodynamic and dynamic environment proximal to WT is also inevitable. For example, at night as the land surface cools by radiative transfer, enhanced vertical mixing induced by WT wakes leads to entrainment of

warmer air from aloft (as manifest in a number of observational studies in large WT arrays, see Table 1), consistent with the historical (and continued) use of wind propellers to prevent freezing of sensitive crops (Battany, 2012). There is also the potential for large-scale deployment of WT to alter surface sensible heat (SH) and latent heat (LH) exchange, near-surface air temperature (*T*) and specific humidity (*Q*), planetary boundary layer height (PBLH), and precipitation (PPT) beyond the edges of WT arrays (i.e., the mesoscale to regional climate). However, the magnitude of possible atmospheric impacts beyond the local scale is subject to considerable uncertainty (see the diversity of results summarized in Table 1). Reducing that uncertainty is the objective of the research presented herein.

First-principle scaling implies there should be greater downstream effects from WT deployed offshore than those located onshore because WSs offshore are more likely to exceed WT cut-in thresholds (i.e., the WS necessary to cause sufficient lift over the rotor plane to generate electricity; Pryor & Barthelmie, 2002) and the near-surface atmosphere is more likely to be stably stratified (leading to more persistent WT wakes; Motta et al., 2005). Further, open water areas lack surface features that can induce vertical motion and enhance vertical transport of higher momentum air from aloft and PBLHs are typically (though not uniformly) lower than over land (Peña et al., 2013). This expectation was realized in idealized simulations with the Weather Research and Forecasting (WRF) model for very large onshore and offshore wind deployments (Volker et al., 2017), and remote sensing observations provide evidence that the WS recovers to within 2% of the free-stream velocity after a distance of 5–20 km downstream of the edge of a large operating offshore WT array (Christiansen & Hasager, 2005). Additionally, first-principle scaling suggests that the impact of WT will tend to be highest when WSs are just above the cut-in (i.e., the WS at which the WT begins to produce electrical power) but below the rated WS (when power production no longer increases with WS, see Figure 1c). In the lower end of WSs in this region, the WT thrust coefficient (i.e., ratio of the thrust force to the dynamic force on the rotor) is largest (Figure 1c), indicating that the relative extraction of momentum from the air is maximized (Manwell et al., 2002). Further, since the turbulence induced by the rotor is also (weakly) dependent on the thrust coefficient, the relative increase in turbulence induced by the rotor will tend to be greatest at low WSs as long as they are above the turbine cut-in (Quarton & Ainslie, 1990). Thus, it is reasonable to expect that in the absence of compensating factors, the climate impacts from WT will be maximized in the season (or times) with moderate WSs (i.e., O[4–7 m/s]) at WT hub height.

The majority of WT (approximately 97%) are installed onshore (Wiser et al., 2016), and therefore, most previous analyses of their climate impacts have focused on land-based WT deployments. These studies have employed a range of approaches to quantify the atmospheric impact of large-scale onshore deployments of WT on the local and downstream atmosphere including in situ measurements, remote sensing instrumentation, and an array of numerical models. Most observational studies have found robust statistical signature of wakes only at relatively short downwind distances from land-based WT arrays (Table 1). Some early numerical research represented the action of WT arrays as large roughness perturbations. More recent numerical simulations at both the global and regional scale represent the action of WTs in a more realistic (though still parameterized) fashion (Fitch et al., 2012; Volker et al., 2015). These parameterizations treat the "far-field" wake (i.e., the wake as observed beyond approximately 3 to 4 WT rotor diameters (*D*) downstream of WT). Studies employing these parameterizations along with in situ measurements conducted downstream of large arrays indicate the effects are of modest magnitude. However, as also illustrated by Table 1, very few numerical studies have used realistic distributions of WT, explicit description of the WT rotor dynamics, and/or have conducted simulations at high resolution over at least a full annual cycle.

Our research is designed to quantify the actual effects from current land-based high-density WT deployments on the mesoscale to regional-scale climate using long-term simulations and robust statistical methods. Our objective is thus to quantify the downstream impact of large WT developments at climate relevant time and space scales using high-resolution (i.e., convection permitting) simulations. We selected a study domain centered over Iowa (in the Central Plains of the United States) because it has the highest WT density of all U.S. states. At the end of 2014 over 80,000 WTs were operating within the contiguous United States and approximately 3,200 were deployed in Iowa (land area ~ 145,000 km^2). Further, Iowa is characterized by relatively flat terrain. It should thus represent an environment in which any downstream impacts from high-density WT arrays might most robustly be simulated and observed.

Journal of Geophysical Research: Atmospheres
10.1029/2017JD028114

Table 1
Précis of a Representative Selection of Previous Research on the Inadvertent Modification of Local to Regional Meteorology by Onshore Deployment of Wind Turbines

Reference	Approach	Domain/ study area	Assumptions/ limitations	Summary of results
Observational studies using in situ measurements and/or ground-based lidars				
C. M. Smith et al. (2013)	In situ measurements using ground-based lidar and anemometers within and downstream of a wind farm	> 200 WT in flat terrain (HH = 80 m)	April and May (mainly unstable conditions)	At 2.1 km downstream: No significant impact on hub height wind speed or turbulence intensity or temperature profiles during daytime; increase in nighttime 2-m air temperature (*T*) by up to 1.6 °C; decrease in daytime 2-m *T* by up to 0.24 °C (not statistically significant)
Rajewski et al. (2016)	In situ surface flux measurements from four stations: two within the wind farm, one at a distance of 450 m upwind of the WT, and one approximately 1 km downwind of the WT.	Two rows of 13 WT in Iowa	Late June to early September	Statistically insignificant difference in daytime *T* under conditions of WT operation, warming of nighttime *T* (0.4 °C)
Armstrong et al. (2016)	In situ measurements at 101 locations with in an operating WF (during operation and curtailment)	54 WT (irregular array) (HH = 72 m)	May–November	Within Wind farm (WF): At night: Close to WT (i.e., up to 200 m downstream) *T* higher by 0.25 °C; specific humidity at 2 m also higher by approximately 0.1 gm^{-3}. At greater distances, *T* slightly suppressed under WT operation. Effects decline logarithmically with distance.
	Observational studies using satellite-based remote sensing			
Harris et al. (2014)	Difference in annual seasonal mean land surface temperature (LST) (computed from 8-day mean LST from Moderate Resolution Imaging Spectroradiometer) 2003–2007 (preconstruction) versus 2009–2013 (postconstruction)	Five wind farms in Iowa		10:30 p.m. differences in LST (°C): wind turbine grid cells MINUS nonwind turbine grid cells (range indicates the range across the five wind farms) MAM: −0.093 to 0.365 JJA: 0.119 to 0.259 SON: 0.181 to 0.485 No signal in winter
Zhou et al. (2012)	Difference in annual seasonal mean LST;	32.1°–32.9°N, 101°–99.8°W domain considered (encompassing	Winter (December–February)	LST in grid cells with WT nighttime temperatures warmer by ≈ 0.7 °C in

Journal of Geophysical Research: Atmospheres

10.1029/2017JD028114

Table 1 *(continued)*

Reference	Approach	Domain/ study area	Assumptions/ limitations	Summary of results
	approach as in Harris et al. (2014)	approximately 2,358 wind turbines)	and summer (June–August)	JJA and ≈ 0.5 °C in DJF (2009–2011 versus 2003–2005); No difference in daytime temperatures. *Note: authors express differences as trends per decade.*
	Wind tunnel study			
Zhang et al. (2013)	Closed-loop thermally controlled boundary layer wind tunnel	Scaled wind turbines in an array of 12 rows and 3 columns		Within wind farm for a neutral boundary layer with a heated surface: Surface heat flux on averaged decreased by approximately 4% relative to flow without WT.
	Numerical modeling: Global scale			
Keith et al. (2004)	Add surface drag to two GCMs: NCAR and GFDL. In three areas encompassing Great Plains (United States), Europe, and China	T42 (approximately 2.8 × 2.8°).	WT remove 40% of kinetic energy of the resolved flow.	"Negligible effect on global mean surface temperature"
Barrie and Kirk-Davidoff (2010)	Large roughness (z_0 = 0.86 m) "patch" (covering 23% of North American land mass) deployed in a global model (CAM3.0)	T42 (approximately 2.8 × 2.8°)	6 years of simulation; described as "theoretical problem"	Step change in roughness grow within 4.5 days such that the flow is altered at synoptic scales resulting in substantial changes in the track and development of cyclones over the North Atlantic.
Wang and Prinn (2010)	CCSM3.0. land areas covered by "grass" replaced by *z*0 of 0.12 (Run 1), 0.16 (Run 2), 0.75 (Run 3), and 2.62 m (Run 4). land areas covered by "shrub" replaced by *z*0 of 0.34 (unchanged), 0.34 (unchanged), 0.34 (unchanged), and 23.45 m.	T42 (approximately 2.8 × 2.8°)	20 years of simulations for each scenario; pseudo "wind farm" deployments restricted to western United States and focused in South America, Africa, and Australia.	Temperature changes (range across grid cells) in lowest model layer Run 1: −0.5 to 0.6 K Run 2: −0.5 to 2 K Run 3: −0.5 to 2 K Run 4: −0.5 to 5.5 K; precipitation was projected to decrease over the northeastern U.S. states by up to 60 mm/yr in Run 1.
Fitch (2015)	Wind farms represented as elevated momentum sinks and turbulence sources in Community Atmosphere Model, version 5 (CAM5)	0.98° latitude × 1.258° longitude	Total installed WT capacity = 2.5 TW (16% of world's projected electricity demand in 2050); large arrays in discrete	Minimal impacts; mean near-surface warming of 0.12 ± 0.07 K is seen within wind farms and an increase in total

Table 1 *(continued)*

Reference	Approach	Domain/ study area	Assumptions/ limitations	Summary of results
			locations around the global 60-year simulations	precipitation rate of +2.6% ± 1.5%. At global scale, mean temperature change of −0.013 ± 0.015 K and precipitation by −0.06% ± 0.09
Numerical modeling: Regional scale				
Vautard et al. (2014)	WRF v3.3.1 with Fitch parameterization applied; resolution of 50 km; ERA-Interim lateral boundary conditions	Europe, 1979–2012	Used actual wind farm locations and where available wind turbine characteristics; also undertook a scenario of enhanced WT deployments	Statistically significant signal for projected WT deployment in 2020 only in winter conditions; magnitudes ±0.3°K for 2-m air temperature and 0–5% for precipitation; high spatial variability in sign and magnitude of differences
Miller et al. (2015)	WRF v3.3.1 with Fitch parameterization; resolution of 12 km	Central Kansas, 15 May to 30 September 2001	Installed capacities of 0.3123 to 100 MW km^{-2} over a 112,320-km^2 area	For a total installed capacity of 561 GW in this area of Kansas the mean wind speed at WTHH in a central grid cell was reduced by 17% in the day and 46% at night.
Baidya Roy et al. (2004)	RAMS; triple nest, 32-8-2 km; WT effect parameterized as increased surface roughness	Central Plains Simulation 1–16 July 1995	Hypothetical wind farm in northern Oklahoma	Within wind farm T2 m increased by 0.7°C, Q2m decreased by 0.7 g/kg

Note. DJF = December–February; MAM = March–May; JJA = June–August; SON = September–November; WT = wind turbine; WRF = Weather Research and Forecasting; HH = hub height; GCMs = general circulation models; NCAR = National Center for Atmospheric Research; GFDL = Geophysical Fluid Dynamics Laboratory.

Journal of Geophysical Research: Atmospheres

10.1029/2017JD028114

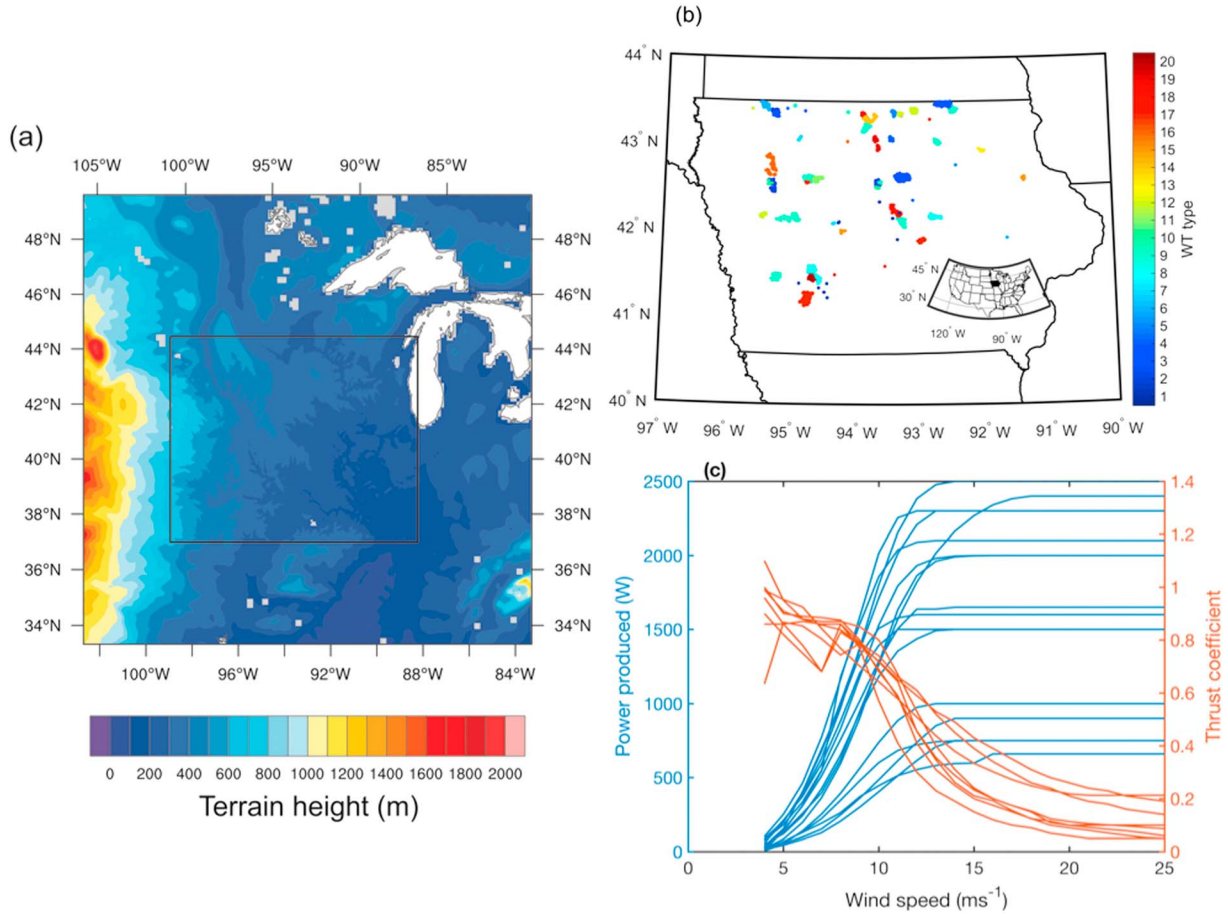

Figure 1. (a) Simulation domains used herein and (b) a map of Iowa (inset shows the contiguous United States with Iowa colored in black) showing the location (dots) and type of wind turbine deployed (colors, see Table 3 for definitions of the WT types). (c) The power curves (blue) and thrust coefficients (red) as a function of wind speed for the 20 WT types used herein. WT = wind turbine.

2. Methods

2.1. Simulations With the WRF Model

The simulations analyzed herein were conducted using the WRF model (v 3.8.1; Powers et al., 2017; Skamarock et al., 2005) and employ the Fitch parameterization to describe the action of WT (Fitch, 2015; Fitch et al., 2012, 2013). In this parameterization the WT act as an elevated momentum sink and a source of TKE, where those effects are imposed in vertical grid cells over which the WT rotor sweeps. The simulations are undertaken using a nested domain configuration that extends from ~103 to 83°W and ~33.5 to 49.5°N. The outer domain (d01) comprises a grid of 149 × 149 grid cells that have a resolution of 12 × 12 km and thus covers an area over 20 times that of Iowa. The inner domain (d02) is resolved at 4 km and comprises 246 × 204 grid cells (see Table 2 and Figure 1a). There are 41 vertical levels up to a model top of 50 hPa, 18 of which are in the lowest 1 km. The lateral boundary (updated 6 hourly and daily) and initial conditions are provided by ERA-Interim reanalysis data (Dee et al., 2011) that have a horizontal resolution of approximately 70 km and National Oceanic and Atmospheric Administration-National Centers for Environmental Prediction (NCEP) real-time global sea surface temperature analyses (Reynolds & Chelton, 2010). The key physics settings employed are shown in Table 2.

The inner domain is simulated at sufficiently high resolution that it is "convection resolving" (Prein et al., 2015), and thus no cumulus parameterization is employed. The decision to undertake the simulations at 4-km resolution (and thus at a scale where convective parameterizations are unnecessary) was made in part because convection parameterization schemes interact nonlinearly with many other parameterization

Table 2
Model Domain Configuration and Physics Settings Used in the WRF Simulations

Simulation settings	Values
Domain size and horizontal resolution (outer domain, d01)	149 × 149 cells, 12 km
Domain size and horizontal resolution (inner domain, d02)	246 × 204 cells, 4 km
Vertical resolution	41 levels up to 50 hPa
Time step for physics	72 s
Physics option	Adopted scheme
Microphysics	5. Eta (Ferrier); Ferrier et al. (2002)
Longwave radiation	1. Rapid Radiative Transfer Model (RRTM; Mlawer et al., 1997)
Shortwave radiation	1. Dudhia (Dudhia, 1989)
Surface layer physics	1. MM5 similarity scheme (Beljaars, 1995)
Land surface physics	2. Noah land surface model (Tewari et al., 2004)
Planetary boundary layer	5. Mellor-Yamada-Nakanishi-Niino 2.5 (Nakanishi & Niino, 2006)
Cumulus parameterization	1. Kain-Fritsch (Kain, 2004; None in d02)

schemes (e.g., planetary boundary layer schemes; Prein et al., 2015) and because the study region is characterized by deep convection during the summer months (Fritsch et al., 1986). Further, wind resource studies require high resolution, and indeed, estimates of the power density at hub height derived using mesoscale models with a 10-km grid spacing can be more than 50% lower than those from higher-resolution models (e.g., Gryning et al., 2014).

Three-dimensional flow fields (e.g., WS) and PBLH and WT power (from the WT run) analyzed herein are output every 10 min. Air temperature at 2 m (T2M), specific humidity at 2 m (Q2M), precipitation (PPT), and the SH and LH fluxes are output hourly. Of the 3-D wind fields we focus our analyses on WSs at 10 m above ground level (agl), from the third model layer (approximately 82 m, which is approximately equal to the mean WT hub height, see Table 3), and from the twelfth model level that equates to an approximate height of 500 m. Output from this latter height is also used to evaluate possible changes in the flow direction and speed. This height is selected based on results from a summertime simulation of central Kansas (15 May to 30 September 2001) for WT installed capacity densities of 0.3125 to 100 MW/km^2 (i.e., 7 to 2500 times the actual value Iowa that is ~0.04 MW/km^2). The simulation of very high WT densities of 5 MW/km^2 indicated a reduction of up to 1.6 m/s in mean nighttime WSs at this height (Miller et al., 2015).

The study domain exhibits pronounced interannual variability in precipitation and temperature (McCabe et al., 2004) and wind regimes (Pryor & Ledolter, 2010; Schoof & Pryor, 2014). Thus, the impact of WT on local to mesoscale climates may also vary from year to year. Calendar year 2008 was selected for use herein because conditions during that year are broadly representative of the climatology of the contiguous United States. After a moderate La Niña in the first half of the year, ENSO-neutral conditions developed by July–August, and temperatures over the contiguous United States during 2008 were close to the climatological normal state, with air temperatures only 0.1 °C above the twentieth century (1901–2000) mean (Peterson & Baringer, 2009). However, June 2008 was characterized by above average rainfall over Iowa and flooding (J. A. Smith et al., 2013).

2.2. WT Description

Following a simulation without any wind turbines (defined here as "no_WT"), the simulation was repeated using the Fitch wind farm parameterization (Fitch et al., 2013) but with all other settings unchanged. In this simulation (defined as "WT"), the locations and types of WTs deployed as of the end of 2014 were obtained from the USGS database (https://eerscmap.usgs.gov/arcgis/rest/services/wind/wTurbinesWMDyn/MapServer) geo-encoded and employed in WRF (see Figure 1b for the WT locations). Where available explicit WT power and thrust curves from the WT manufacturers were used, while power and thrust curves were derived for all remaining WT using scaled values (Table 3). The total installed capacity in Iowa from these georeferenced WT is 5.18 GW (representing the installed capacity as of the end of 2014, for comparative

Table 3
The Most Common Types of Wind Turbines in the Database for Iowa as of the End of 2014 and the Turbine Descriptive Parameters Used Within the Fitch Parameterization

Rank	Machine manufacturer and model	# of WT	Hub height (HH; m)	Rotor diameter (D; m)	Power (P) and/or thrust (c_t) curves	Rated capacity (RC; MW)
1	GE 1.5 SLE	781	80	77	Explicit	1.5
2	Vestas V82	443	80	82	Explicit	1.65
3	Zond Z50	260	63	50	Averages from WT with equal RC	0.75
4	Siemens 2.3_101	258	80	101	Taken from similar Bonus machine	2.3
5	GE 1.5 S	236	64.7	70.5	P from 1, c_t explicit	1.5
6	Siemens 2.3_108	195	80	108	P, c_t from #4	2.3
7	Gamesa G87	172	78	87	P, c_t average from WT with equal RC	2
8	Vestas V47	151	65	47	P, c_t from #2	0.6
9	GE 1.5 XLE	145	80	82.5	P, c_t from #1	1.5
10	NEG Micon NM 52_900	90	100	52.2	Scaled from 2 MW	0.9
11	Clipper C99	80	80	99	Used #13	2.5
12	Siemens SWT 2.3_93	76	80	93	P, c_t from #14	2.3
13	Clipper C96	61	80	96	P, c_t average from WT with equal RC	2.5
14	NEG Micon NM 48_750	57	55	48	Scaled from 2 MW	0.75
15	Mitsubishi MWT 1000A	50	68	61.4	Explicit	1
16	Gamesa G97	40	100	97	P, c_t average from WT with equal RC	2.0
17	Nordex N100	37	100	99.8	Scaled P from Nord2500, c_t average from WT with equal RC	2.4
18	Suzlon S88	17	80	88	P, c_t average from WT with equal RC	2.1
19	GE 1.6_82.5	17	80	82.5	P, c_t scaled from GE 1.7 MW	1.6
20	Nordex N117	15	91	117	Scale P from Nord2500, c_t average from WT with equal RC	2.4

Note. This list accounts for 3,181 of 3,218 turbines (98.9%) in IA. WT = wind turbine.

purposes the value at the end of 2017 was approximately 6.92 GW). The two most common WT types as deployed in Iowa at the end of 2014 were the GE 1.5SLE and Vestas V82, both of which have a hub height of 80 m (Table 3). Accordingly, the mean WT hub height in Iowa as of the end of 2014 is approximately 78 m (relative to the current national mean value of 83 m; Wiser & Bolinger, 2017) and the mean rated power is 1.6 MW. These WTs are not evenly distributed across the state (see Figure 1b), highlighting the importance of studies such as that conducted herein that accurately geolocate WT and use their actual rotor dimensions and dynamics (Table 3 and Figure 1c) in order to quantify climate impacts.

2.3. MERRA-2 and NARR

The WRF simulations presented herein are conducted using ERA-Interim lateral boundary conditions. Thus, there is an expectation that the large-scale atmospheric state within the simulation domain will be reasonably represented by the WRF model. Fidelity of the no_WT simulation with WRF is performed here using two reanalysis products. Simulations of some of the key climate parameters considered herein, that is, air temperature at 2-m (T2M), specific humidity at 2-m (Q2M), precipitation (PPT), PBLH, and the atmosphere-surface exchange of SH and LH are evaluated and contextualized using output from the Modern-Era Retrospective Analysis for Research and Application, version 2 (MERRA-2; Buchard et al., 2017; Randles et al., 2017). Given the importance of grid resolution and data assimilation to variables such as precipitation, PBLH, and near-surface WS, these variables are also evaluated using output from the North American Regional Reanalysis (NARR; Mesinger et al., 2006). MERRA-2 is derived using assimilation of both meteorological and aerosol observations every 6 and 3 hr, respectively, into the Goddard Earth Observing System, version 5 model (Molod et al., 2015). It provides hourly, global gridded output of the aforementioned meteorological variables at 0.625° by 0.5° resolution. NARR output is available 8 times per day at a resolution of approximately 32 by 32 km and is generated using data assimilation into the very high resolution NCEP Eta model.

2.4. Statistical Methods

Since the research presented herein is designed to examine climate impacts (i.e., modifications of the atmosphere that are manifest over relatively long time frames), the majority of the analyses of simulation fidelity and WT impacts are conducted by climatological season (winter; December, January and February [decfeb]),

Table 4
Précis of Seasonal Mean Values of Key Climate Parameters in d01 and d02 From MERRA-2 and the no_WT WRF Simulation

	Winter: DJF		Spring: MAM		Summer: JJA		Fall: SON	
Variable	MERRA-2: d01/d02	WRF: d01/d02	MERRA-2: d01/d02	WRF: d01/d02	MERRA-2: d01/d02	WRF: d01/d02	MERRA-2: d01/d02	WRF: d01/d02
T (K)	271/269	270/269	282/282	282/283	295/296	295/297	284/284	284/285
Q (g/kg)	2.8/2.8	2.6/2.5	5.4/6.0	5.0/5.4	11.3/12	11.1/11.3	6.3/6.8	6.4/6.4
PPT (mm)	176/124	171/139	248/227	303/315	264/239	525/276	184/174	207/222
PBLH (m)	482	478	845	757	962	780	639	621
SH (W/m^2)	6.0/8.0	27/20	44/38	62/58	53/45	52/58	26/22	31/38
LH (W/m^2)	16/19	20/17	64/73	58/71	102/113	102/113	38/46	44/33
	NARR d02	WRF d02	NARR d02	WRF d02	NARR d02	WRF d02	NARR d02	WRF d02
PPT (mm)	159	139	333	315	344	276	216	222
PBLH (m)	720	478	944	757	903	780	774	621
WS (at 10 m) (m/s)	4.93	5.44	4.91	5.49	3.88	4.26	4.42	4.77

Note. *T* = Mean air temperature (at 2 m), *Q* = Mean specific humidity (2 m), PPT = mean seasonal total precipitation, PBLH = mean planetary boundary layer height, SH = mean sensible heat flux, LH = mean latent heat flux. PBLH is only shown for d02. The lowest three rows show mean seasonal total precipitation, PBLH and mean wind speed at 10 m (WS10) within d02 from the North American Regional Reanalysis (NARR, 32 km resolution) and the WRF no_WT simulations presented herein. DJF = December–February; MAM = March–May; JJA = June–August; SON = September–November; WRF = Weather Research and Forecasting; HH = hub height; WS = wind speed; MERRA-2 = Modern-Era Retrospective Analysis for Research and Application, version 2.

spring (March–May [marmay]), summer (June–August [junaug]), and fall (September–November [sepnov]). Output from the no_WT simulation is first evaluated by comparing seasonal mean conditions integrated over the areas covered by d01 and d02 relative to values from MERRA-2 and NARR (see Table 4) to provide an overview of the simulation fidelity. Then the impact of WT operation on the regional climate of Iowa and the surrounding states is quantified using the following four approaches:

1. The mean difference in output from the paired simulations (WT minus no_WT) for the following key variables: T2M, Q2M, PPT, PBLH, WS10, and WS at WT hub height (i.e., from the model layer at approximately 82-m height), and WS at the model layer closest to 500 m height (WSHH and WS500, respectively) is computed from the time series and shown graphically grid cell by grid cell. For the WS and PBLH this calculation is conducted using output every 10 min, while for all other variables once hourly values are used.
2. The median value of each variable in the WT simulation in each grid cell is computed and compared to the 2.5th and 97.5th percentile median values computed from a bootstrapped sample (of sample size n = 1,000) of the no_WT time series. This analysis is thus testing, for example, whether the median value of the air temperature at 2 m in that grid cell for the WT simulation could reasonably be expected to occur in the no_WT simulation. If the median value of the T2M, Q2M, SH, or LH in the WT simulation for that grid cell lies beyond these 95% bootstrapped confidence intervals from the no_WT simulation, conditions in that grid cell are deemed to be significantly impacted by the presence of WT.
3. In the case of precipitation we assess the frequency of precipitation in each grid cell with a difference of proportions test (i.e., H_0: $\pi_1 = \pi_2$, where π_1 is the probability of precipitation in any hour in the no_WT simulation and π_2 is the probability of precipitation in any hour in the WT simulation) using a Z statistic computed as follows:

$$Z = \frac{\pi_1 - \pi_2}{p(1-p)\left(\frac{1}{n_1} + \frac{1}{n_2}\right)}$$

where $p = \frac{X_1 + X_2}{n_1 + n_2}$, and X_q, n_q, and π_q are the number of occurrence of precipitation, the total number of hours, and proportion of hours with precipitation in the two simulations (q = 1:2), respectively.

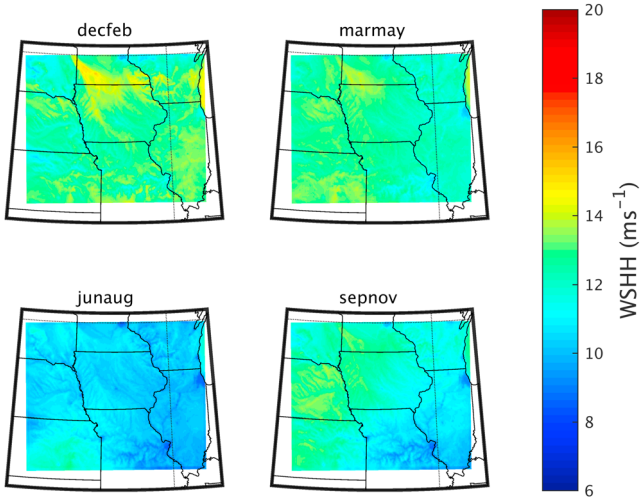

Figure 2. Grid cell mean wind speeds in each climatological season (from upper left to lower right: winter, spring, summer, and fall) at/close to the mean WT hub height (i.e., approximately 83 m above ground level) in d02 from the no_WT simulations of 2008. WT = wind turbine.

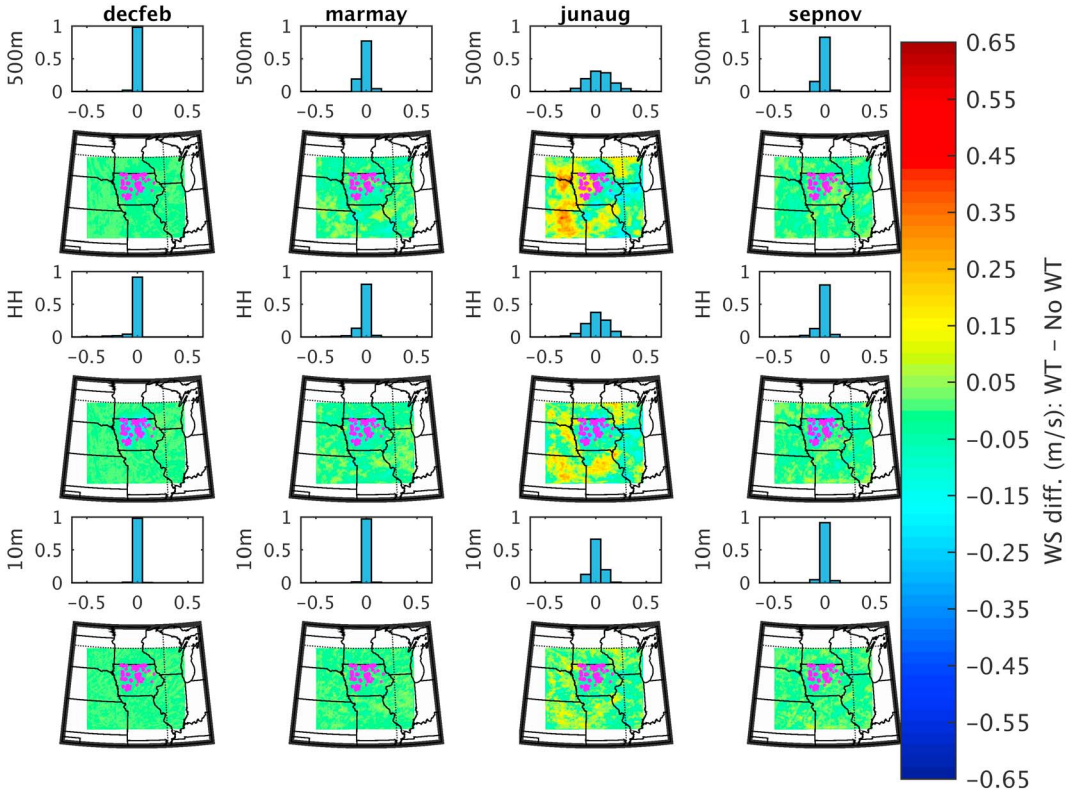

Figure 3. Grid cell mean differences in wind speeds in d02 from the WRF simulations (WT minus no_WT). The three rows show the three heights from which wind speeds are considered: (top row) 500 m, (middle row) close to wind turbine hub height, and (bottom row) 10 m. The columns denote the different seasons. The histogram is derived from the spatial maps and shows the frequency distribution of mean differences (discretized in 0.1-m/s intervals) across the 246 by 204 grid cells; the map then shows the results spatially. The magenta points on the maps indicate the locations of WT. WRF = Weather Research and Forecasting; WT = wind turbine.

Repeated applications of any statistical test at any significance level (α) will cause false positives and the family-wise error rate (FWER) scales with the number of repetitions (k):

$$\mathrm{FWER} = 1 - (1 - \alpha)^k$$

Hence, probabilities associated with each statistical score (i.e., each grid cell [p_j]) are computed and ranked from low to high (j = 1 to k, where k is the total number of grid cells). The results of individual tests are significant for all grid cells in which the following is true (Wilks, 2011):

$$p_j \leq \frac{j}{k}\alpha$$

4. There is considerable grid cell to grid cell variability in the sign and magnitude of differences (WT minus no_WT) in precipitation, and intense convective precipitation makes a large contribution to annual total precipitation in Iowa (Fritsch et al., 1986). Thus, cumulative density functions (CDF) of the difference in total precipitation (WT minus no_WT) are also compared for each season for hours during which any precipitation occurred in the no_WT simulation and for hours in which high precipitation amounts were simulated.

3. Results

3.1. Evaluation of the no_WT simulation

Output from the no_WT simulation exhibits very similar values for seasonal average air temperature and specific humidity with those from MERRA-2 (Table 4) but is wet biased in d02 relative to MERRA-2 during spring

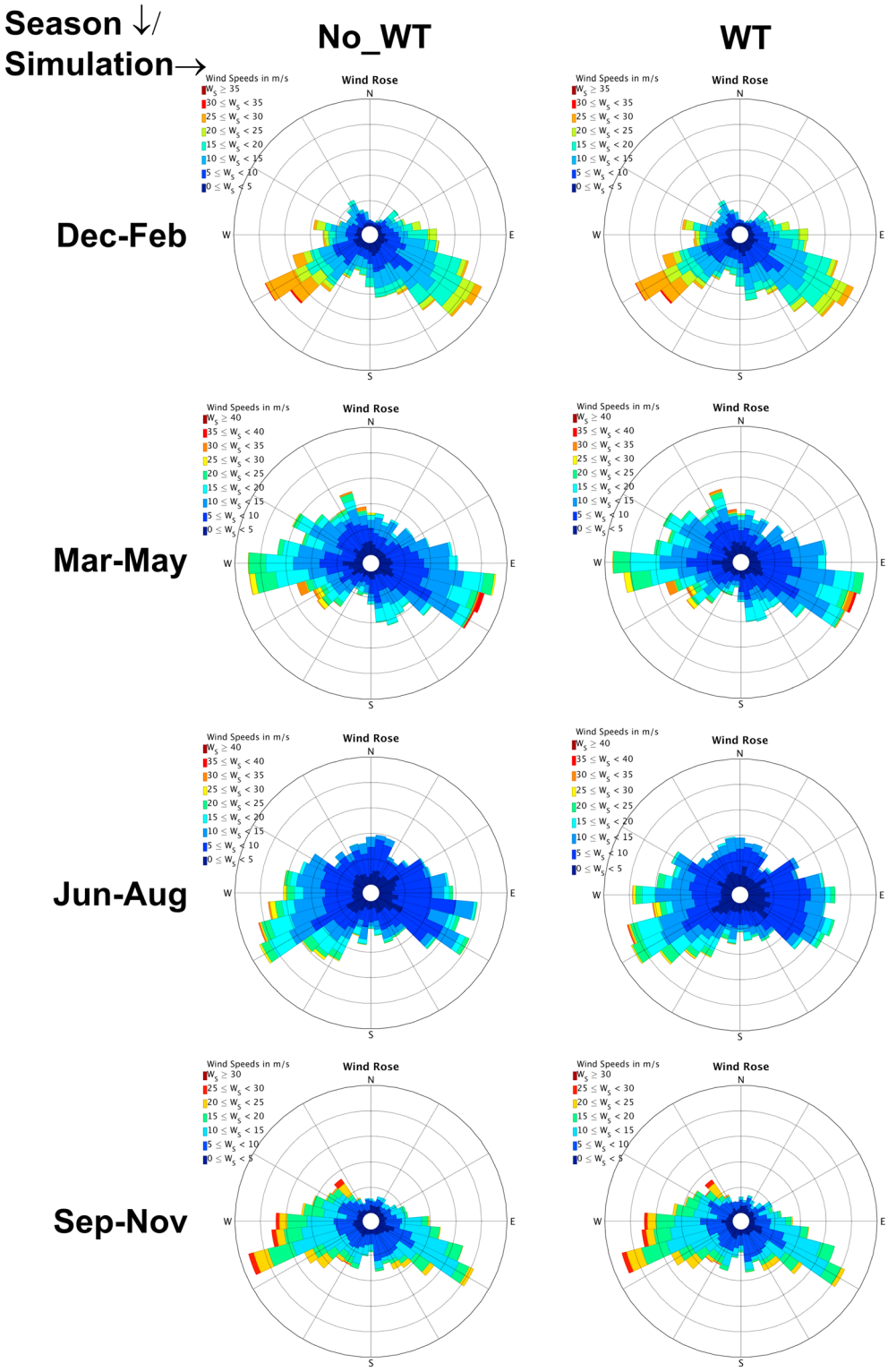

Figure 4. Seasonal wind roses of 10-min wind speed and direction at approximately 500 m above ground level from a single grid cell in the center of Iowa. The 10-min output from the no_WT and WT simulations are discretized into 10° directional sectors and 5-m/s speed intervals. WT = wind turbine.

and summer. However, observations from 15 National Weather Service-Automated Surface Observing System stations in Iowa indicate mean seasonal totals of 116, 315, 396, and 213 mm (for winter-fall, respectively), while those form NARR are 159, 333, 344, and 216 mm (Table 4). Further, MERRA-2

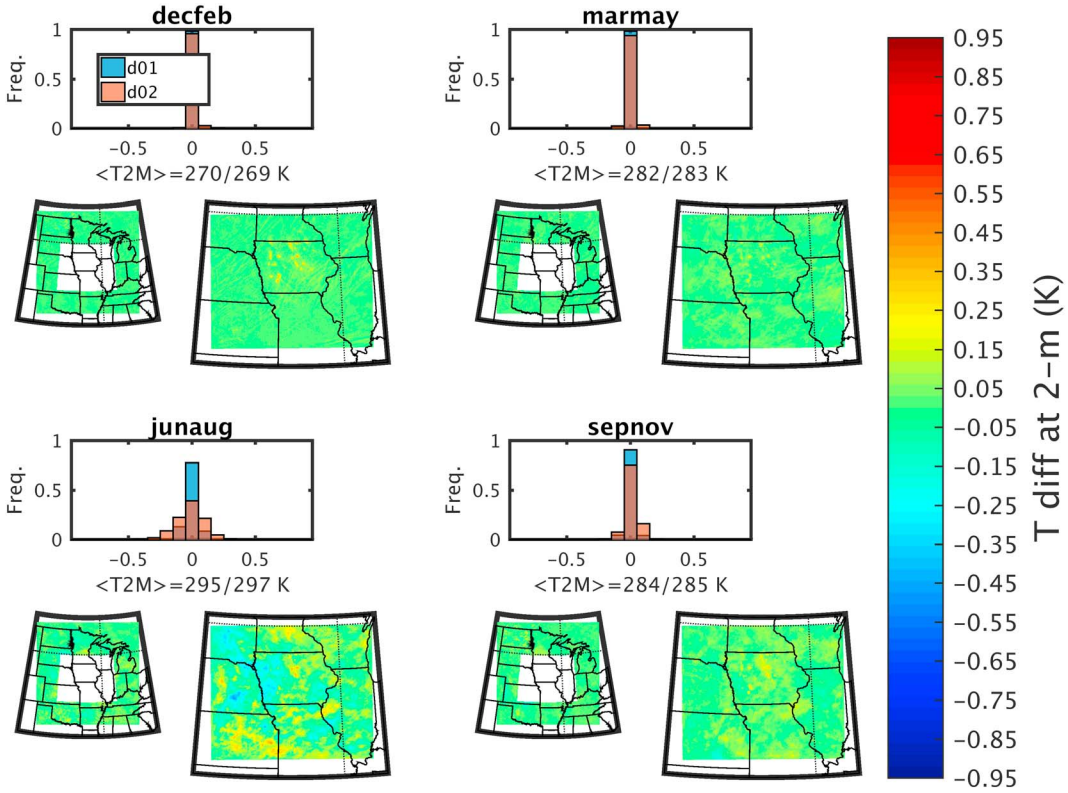

Figure 5. Grid cell mean differences in air temperature at 2 m (T2 m) from the WRF simulation with wind turbines minus the no_WT simulation. Each panel shows a different season (decfeb = winter, marmay = spring, junaug = summer, sepnov = fall). In each panel the histogram denotes the number of grid cells that exhibit a difference of a given magnitude (discretized in 0.1 K intervals), the lower left map shows d01 with the inner domain (d02) masked out, and the right-hand map shows the inner domain (d02). The values below each histogram indicate the domain average T2 m in d01 (with d02 masked out)/d02 in that season. The scales used in each subplot are consistent across all seasons. WRF = Weather Research and Forecasting; WT = wind turbine.

precipitation estimates for the eastern United States during 2008 have previously been reported to exhibit a negative bias (i.e., precipitation totals are too low; Reichle et al., 2017). Thus, the seasonal mean PPT from the WRF no_WT simulation is within the range between the MERRA-2, NARR, and in situ observational estimates, and therefore, the precipitation estimates from WRF were deemed sufficiently skillful to be included in the analysis of climate impacts of WT in Iowa. However, it is noted that precipitation amounts and intensity as generated by numerical weather prediction models exhibit a high sensitivity to resolution (Sun et al., 2014) and the simulation settings particularly during the warm season (Gallus Jr & Bresch, 2006).

Both the SH and LH fluxes from the no_WT simulation are positively biased relative to estimates from MERRA-2 in winter and spring but exhibit closer accord in summer and fall. These values are less well constrained in the MERRA-2 reanalysis than other variables (i.e., there is no assimilation of data representing these energy fluxes). Further, surface-atmosphere fluxes also exhibit a strong scale dependence (LeMone et al., 2007). Thus, while the discrepancies in these flux estimates must be considered when evaluating the robustness of any WT impacts on regional climate, the simulations were also deemed adequate to provide a first estimate of possible impacts on these energy balance components.

PBLH is a key variable for dictating the impact of WT on near-surface climate since it effectively dictates the volume of air from which momentum can be extracted. However, PBLH is highly sensitive to the physical schemes applied, and biases appear to be domain and resolution dependent (e.g., Xie et al., 2012). Additionally this parameter is comparatively difficult to evaluate in part because of differences in how PBLH is diagnosed (Schmid & Niyogi, 2012). For example, PBLH is computed from heat diffusivity in MERRA-2, but TKE in WRF and a diagnostic formula using equilibrium TKE in NARR. Thus, they are not strictly comparable. The spatial average mean PBLH in winter for d02 from WRF and MERRA-2 is virtually identical but is lower than estimates from NARR. WRF no_WT estimates are negatively biased relative to MERRA-2 and

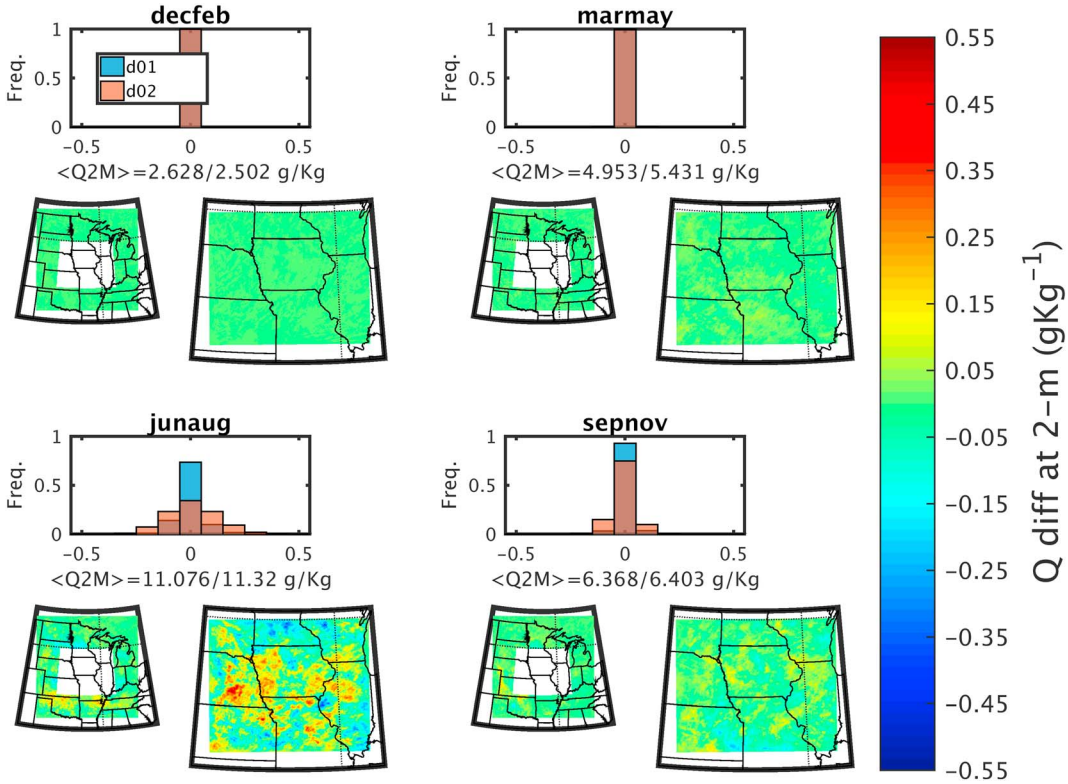

Figure 6. Grid cell mean differences in specific humidity at 2 m (Q2M) from the WRF simulation with wind turbines minus the no_WT simulation. Each panel shows a different season (decfeb = winter, marmay = spring, junaug = summer, sepnov = fall). In each panel the histogram denotes the number of grid cells that exhibit a difference of a given magnitude (discretized in 0.1-g/kg intervals), the lower left map shows d01 with the inner domain (d02) masked out, and the right-hand map shows the inner domain (d02). The values below each histogram indicate the domain average Q2M in d01 (with d02 masked out)/d02 in that season. The scales used in each subplot are consistent across all seasons. WRF = Weather Research and Forecasting; WT = wind turbine.

NARR for the other seasons (Table 4), which may lead to an artificial amplification of the WT effect on downstream climate due to negative bias in the volume of air from which momentum can be extracted and into which the additional TKE is injected.

WSs at/close to the WT hub heights in Iowa exhibit a seasonal cycle, with higher mean WSs during winter and lowest mean WSs during summer (Figure 2). The spatial patterns in these WS maps, with higher values in the western half of the state, are consistent with resource estimates available from the U.S. National Renewable Energy Laboratory (accessible from https://windexchange.energy.gov/maps-data?height=80m) and are also reflected in the spatial distribution of WT (Figure 1b). Consistent with previous research that has indicated a negative bias in 10-m WSs from NARR (Pryor et al., 2009), mean seasonal WSs from the no_WT WRF simulation exhibit similar seasonality to NARR but higher absolute values in d02 of up to 0.5 m/s (Table 4).

As a result of the seasonality in WSs the seasonal average gross capacity factors (CFs, i.e., the ratio of the domain total simulated electrical power produced by the Fitch parameterization to the rated power for all WT) are 52, 50, 33, and 48% for winter, spring, summer, and fall, respectively. These gross CF values are higher than typical observed CFs because the analysis assumes 100% WT availability (i.e., no downtime for maintenance and no curtailment of production due to availability of excess power on the electrical grid). Actual annual average observed CFs for WT deployed in the United States, which also include the influence of curtailment on electrical power production, have increased as the technology has evolved and are 42.5% for WT installations commissioned during 2016 (Wiser & Bolinger, 2017). Curtailment of wind power production over the period 2007–2012 within the Midcontinent Independent System Operator region in which Iowa is located ranged from 1 to 4% when expressed as a fraction of wind generation (Bird et al., 2014). Exclusion of WT curtailment from the simulations will likely result in a small inflation of the impact of WT on local to mesoscale climate.

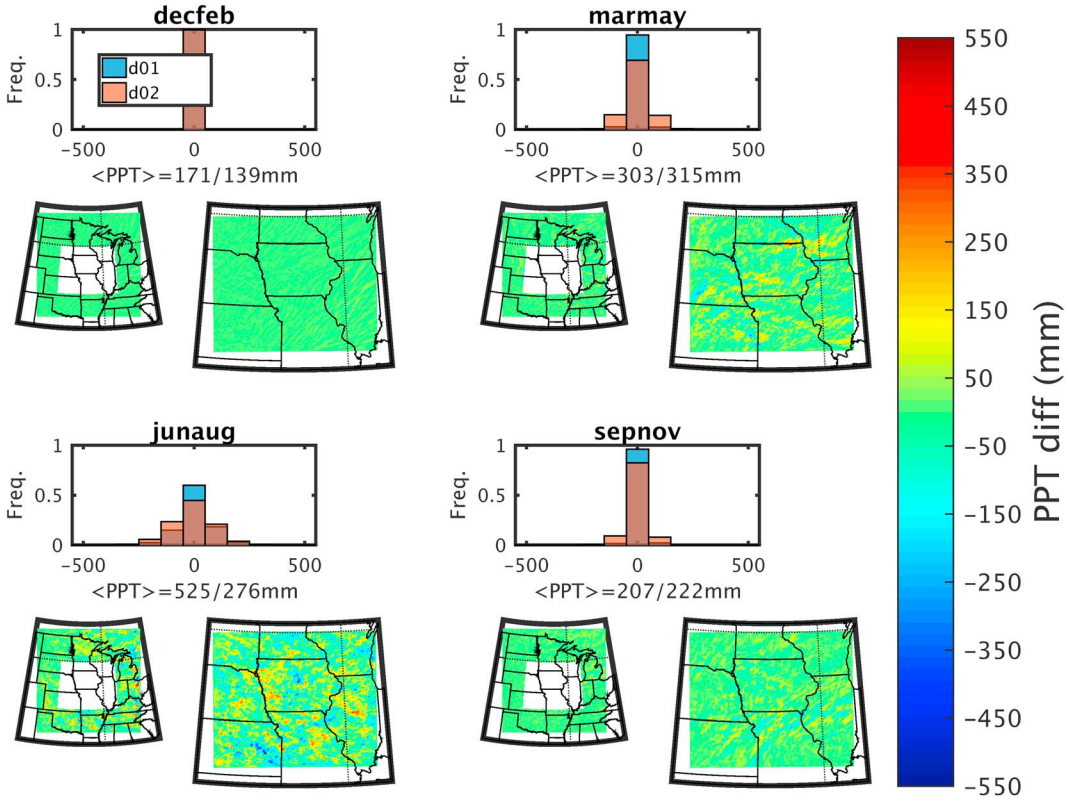

Figure 7. Grid cell differences in seasonal total precipitation (PPT) from the WRF simulation with wind turbines minus the no_WT simulation. Each panel shows a different season (decfeb = winter, marmay = spring, junaug = summer, sepnov = fall). In each panel the histogram denotes the number of grid cells that exhibit a difference of a given magnitude (discretized in 100-mm intervals), the lower left map shows d01 with the inner domain (d02) masked out, and the right-hand map shows the inner domain (d02). The values below each histogram indicate the average PPT in d02 and the mean perturbation in d02 in that season. The scales used in each subplot are consistent across all seasons. WRF = Weather Research and Forecasting; WT = wind turbine.

3.2. Climate Impacts of WT

In the following sections we consider the impact of WT in Iowa on atmospheric properties within the simulation domain. We evaluate the perturbation of the climate variables in terms of the pairwise differences in output from the WT and no_WT simulation.

3.2.1. Impacts on Flow Conditions

Consistent with the discussion above regarding the aerodynamics of WT rotors, and specifically the dependence of the thrust coefficient on WS (Figure 1c), the perturbation of 10-m WSs and those in the layer closest to the mean WT hub height are also largest in the summer and have maximum values of ~ 0.3–0.5 m/s in individual grid cells (Figure 3). Summer WSs at all three heights are generally lower in grid cells with operating WT in them, but there are important compensating effects at distance downstream. For example, WSs at 500 m toward the western edge of d02 are actually higher on average in the WT simulation. This is potentially due to the enhanced vertical coupling in this simulation and thus momentum transfer from aloft, due in part to higher SH fluxes (see discussion below) and TKE introduced by the WT parameterization. The difference in WSs in grid cells containing WT for the WT and no_WT simulations indicates a mean (spatially averaged) difference in d02 during winter < -0.01 m/s at 10 m agl, -0.02 m/s near WT hub height, and -0.01 m/s at 500 m. During summer, which is the season in which the WT simulation differed most from the no_WT simulation, the respective mean differences (averaged in time and space) in d02 are <0.01 m/s at 10 m and WTHH and WS at approximately 500 m differ by an average of 0.04 m/s.

Wind roses constructed from time series of 10-min WSs and wind directions at a height of approximately 500 m from a central grid cell in d02 (that does not contain WT) are virtually identical for the no_WT and WT simulations during winter, spring, and fall, indicating that the impact of the WT on this simple representation of the circulation patterns is negligible (Figure 4). In accord with the précis given in Figure 3, the only

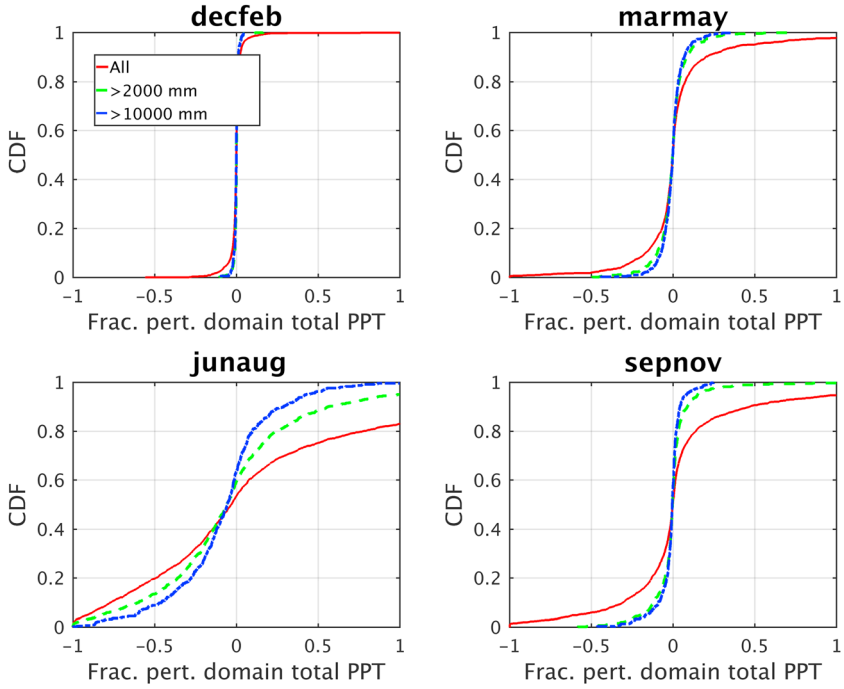

Figure 8. Cumulative density function (CDF) of the perturbation of domain total hourly precipitation in d02 for all hours in which any precipitation occurred in the no_WT simulation (denoted as all in the legend) and for threshold values of 2,000 mm and 10,000 mm. A value of ±0.5 indicates a 50% difference in precipitation during that hour between the paired sets of simulations, where a positive value indicates the WT simulation exhibited a higher precipitation total in d02 than the no_WT simulation. WT = wind turbine.

season in which the wind roses for a central grid cell in d02 indicate substantial perturbation of the flow pattern at 500 m is summer (Figure 4). During summer, in addition to an increased prevalence of the lower WS classes, the frequency of easterly and southeasterly flow is lower in the WT simulations while the frequency of westerly winds is higher (Figure 4).

These findings are in accord with a priori expectations based on the WT thrust coefficients (see examples in Figure 1c) and knowledge that the WS regime in summer is characterized by lower speeds than during the other seasons (Figures 2 and 4). WSs at WT hub heights typically remain above WT cut-in WSs during summer (i.e., when the WT begins to extract momentum and generate electrical power at a rate described by the power curve) but are of a magnitude that is associated with high thrust coefficients. Thus, the WT act in a manner that maximizes both the relative extraction of momentum and the addition of rotor-induced turbulence. Although there are large impacts on WSHH in individual grid cells with mean reductions of up to 0.5 m/s during summer, the impact on the regional flow field is small. This is consistent with direct observational evidence that, under moderate turbulence intensities, the velocity deficit that defines WT wakes is clearly evident only to downwind distances of up to 8 times the rotor diameter from individual turbines (which would equate to an average downstream distance for the WT used herein of ~ 1 km; C. M. Smith et al. 2013).

3.2.2. Impacts on Other Atmospheric Properties

The mean differences in T2M, Q2M, PPT, PBLH, LH, and SH between the WT and no_WT simulations are of modest magnitude both in individual grid cells and averaged over both d01 and d02 (see Figures 5–11). The lack of coherent impact on grid cells within the outer domain is symptomatic of effects that are localized to the inner domain (d02) in which the effects of WT are parameterized and is also in accord with observational studies (Table 1). For this reason only perturbations within d02 are described in detail below.

During winter the presence of WT has very little impact on all the variables considered. For example, the maximum difference in T2M in any grid cell within d02 during the winter season is 0.39 K. The domain average spatial mean and median of the grid cell mean differences is $<$0.01 K (Figure 11), and interquartile range of grid cell mean differences is $-$0.007 to 0.012 K. The mean differences during spring and fall in T2M, Q2M, and PPT between the WT and no_WT simulations are also small (i.e., $<$ 1% of the grid cell mean values in the

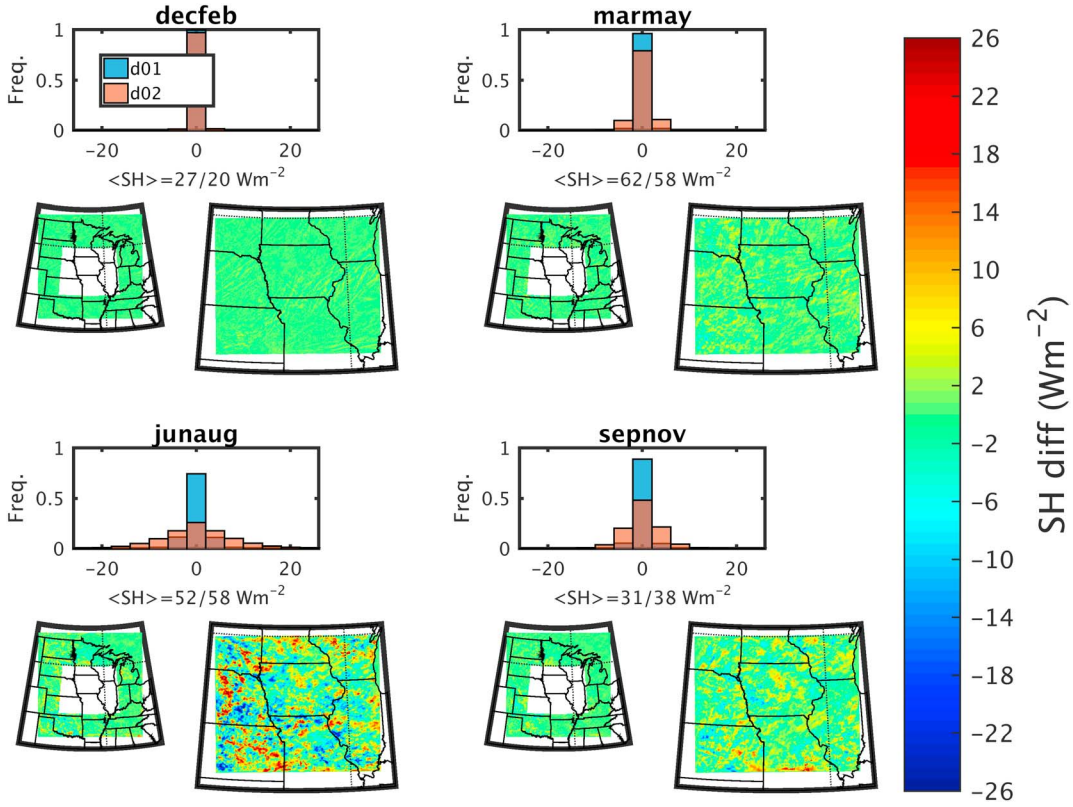

Figure 9. Grid cell differences in the mean SH flux from the WRF simulation with wind turbines minus the no_WT simulation. Each panel shows a different season (decfeb = winter, marmay = spring, junaug = summer, sepnov = fall). In each panel the histogram denotes the number of grid cells that exhibit a difference of a given magnitude (discretized in 4 W/m^2-intervals), the lower left map shows d01 with the inner domain (d02) masked out, and the right-hand map shows the inner domain (d02). The values below each histogram indicate the mean SH in d01 and d02. The scales used in each subplot are consistent across all seasons. WRF = Weather Research and Forecasting; WT = wind turbine; SH = sensible heat.

no_WT simulation; Figures 5–7). The impact of WT in near-surface air temperatures (T2M) is slightly greater in fall than spring (Figure 5), likely because the fraction of WT rotor-induced turbulence (and enhanced vertical mixing) is higher in fall than spring (i.e., higher thrust coefficients in fall due to the lower WSs lead to larger TKE injection into the atmosphere; Figures 1 and 2). The maximum difference in T2M (recall all differences are computed pairwise in the time series for each grid cell) in any grid cell is almost +0.5 K (with air temperatures in the WT simulation being warmer than in that grid cell in the no_WT simulation). However, as shown in Figure 5, histograms of the grid cell differences are almost symmetric around 0 in both d01 and d02, indicating that the localized areas of net cooling and net warming are in balance when considered over the entire simulation domain. Accordingly, the domain average effect for summer is almost zero ($<$ |0.01| K) and interquartile range of grid cell mean differences is $-$0.079 to 0.056 K. During the other seasons, the presence of WT leads to smaller net differences in grid cell mean T2M but a slight tendency toward warming when spatially averaged over d02 (of $<$0.1 K).

Although the primary focus of our research is assessing the seasonality of WT impacts on the regional climate, the WT parameterization also captures the magnitude, sign, and diurnal cycle of local impacts on near-surface air *T* that have been reported in observational studies (Table 1). For example, in simulations with WT present, 88% and 76% of grid cells exhibit T2M during the wintertime nighttime hours (midnight to 6 a.m., inclusive) and daytime hours (11–5 p.m., inclusive) that are $>$0.1 K warmer than in the no_WT simulation. No grid cells exhibit differences that exceed 0.5 K during either the nighttime or daytime hours. The respective values for summer are 86% (night) and 22% (day) for a threshold of 0.1 K, and 4% of grid cells with WT exhibit nighttime warming in excess of 0.5 K. However, consistent with in situ measurements (Table 1), these effects are largely confined to the 16 km^2 grid cells in which WTs are located. When grid cells that do not contain WT are selected, less than 1% exhibits mean differences (WT minus no_WT) in T2M in

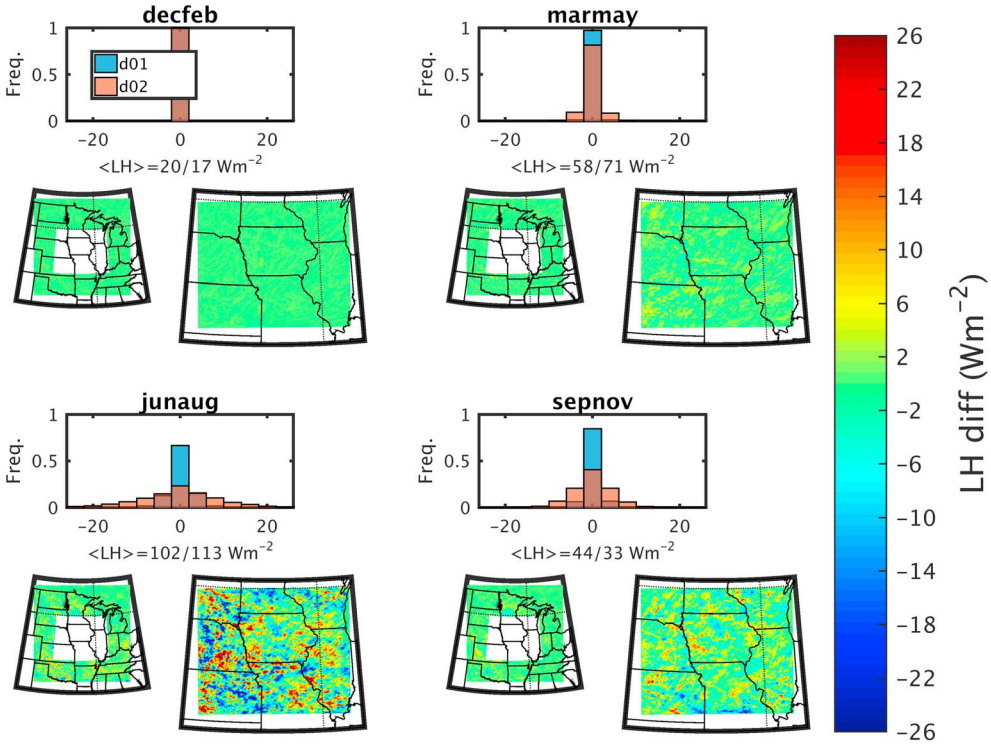

Figure 10. Grid cell differences in the mean LH flux from the WRF simulation with wind turbines minus the no_WT simulation. Each panel shows a different season (decfeb = winter, marmay = spring, junaug = summer, sepnov = fall). In each panel the histogram denotes the number of grid cells that exhibit a difference of a given magnitude (discretized in 4 W/m^2-intervals), the lower left map shows d01 with the inner domain (d02) masked out, and the right-hand map shows the inner domain (d02). The values below each histogram indicate the mean SH in d01 and d02. The scales used in each subplot are consistent across all seasons. WRF = Weather Research and Forecasting; WT = wind turbine; LH = latent heat; SH = sensible heat.

nighttime or daytime hours that exceed 0.1 K during winter. During summer approximately one third of all grid cells exhibit differences during both daytime and nighttime hours that exceed $>\pm0.1$ K, and they are equally distributed between positive and negative values. No grid cells exhibit mean differences in T2M during summer nighttime or daytime hours that exceed $|0.5|$ K.

The largest impact of WT on near-surface specific humidity is also observed in summer (Figure 6). In summer the interquartile range of grid cell mean differences is -0.07 to 0.08 g/kg, but some grid cells indicate mean Q2M in the WT simulation that exceed the no_WT simulation by up to 0.4 g/kg (this equates to up to a 4% increase in Q2M in some grid cells, especially those close to WT). However, in all other seasons the impact is more modest (i.e., $<1\%$ of value in the no_WT simulation). In all seasons apart from summer fewer than 5% of grid cells exhibit median Q2M values in the WT simulation that lie outside the 95% bootstrapped confidence intervals on the no_WT simulation (Figure 11). During the summer 11% of grid cells indicate that the median Q2M value from the WT simulation lies beyond those confidence intervals and the spatially averaged difference is almost 0.02 g/kg (Figure 11).

In terms of precipitation (Figures 7 and 8) and both the LH and SH fluxes (Figures 9 and 10), the patterns of grid cell differences are much less spatially coherent. The presence of WT in the simulation slightly decreases the d02 total precipitation for winter, spring, and fall, but the seasonal mean perturbation is $<0.6\%$ ($<$ 1 mm), which is much smaller than the simulation uncertainty. The probability of precipitation is unaltered in winter (based on analysis of *Z* scores), with fewer than 5% of grid cells resulting in rejection of the null hypothesis that the difference in the probability of precipitation is zero at a significance level of 0.05. For the summer season, the WT simulation exhibits a mean perturbation of seasonal total precipitation of -2.6% (approximately 7 mm, Figure 7), and the *Z* scores for probability of precipitation are significantly different to zero for almost one-quarter of grid cells. However, simulated precipitation is known to exhibit both a high sensitivity to lateral boundary conditions and a comparatively large stochastic

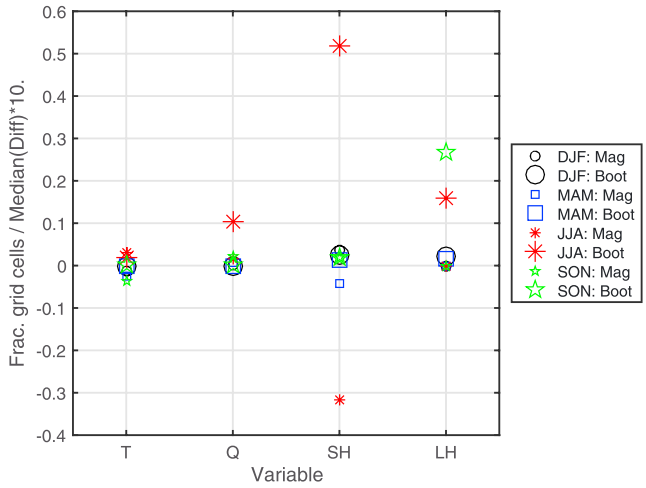

Figure 11. Précis of the statistical tests on the thermodynamic variables in d02 as simulated in the no_WT and WT runs. The results are presented by climatological season (DJF = winter, MAM = spring, JJA = summer, and SON = fall). For each season two statistics are presented; Mag indicates the median difference (i.e., the spatial average of the grid cell specific median values) multiplied by a factor of 10 (so a median difference value of 0.05 would be plotted as 0.5). The units of these differences are as in the variable considered, that is, T (k), Q (g/kg), and W/m^2 for SH and LH. Boot indicates the fraction of the total grid cells within d02 in which the median value from the WT simulation lays beyond 95% bootstrapped confidence interval computed from the no_WT simulation corrected for field significance. DJF = December–February; MAM = March–May; JJA = June–August; SON = September–November; WT = wind turbine.

component. This, and the lack of spatial coherence in the precipitation difference fields (Figure 7), imply effects of this magnitude cannot be robustly detected within a single year of simulations. The CDF of the domain total precipitation perturbations (pairwise differences of hourly d02 total PPT) for all seasons except summer crosses the zero point at approximately the median, indicating an equal fraction of hours that exhibit higher and lower precipitation in the WT and no_WT simulations (Figure 8). The fractional perturbation of domain total hourly precipitation scales with the magnitude of the precipitation events during the summer and, to a lesser extent, during spring and fall. For large magnitude events (those exceeding 10,000 mm over d02, which equates to about 25% of the hours on which precipitation is observed during summer) less than 20% of hours exhibit fractional perturbation amounts in excess of 50%. Thus, the large fractional impacts on precipitation appear to be largely confined to hours with small magnitude or spatially confined precipitation events. In summer, there is a clear tendency for the perturbation of domain total precipitation within a given hour to be negative. Indeed, for hours in which more than 10,000 mm of precipitation occurred in d02 (i.e., the spatial total of precipitation amounts over this threshold), 60% of the perturbations are negative. This implies that the presence of WT is associated with a decrease in domain total PPT during 60% of hours when substantial precipitation occurred.

SH and LH fluxes exhibit strong seasonality, as does the WT impact on the spatial patterns of these fluxes (Figures 9–11). The LH and SH fluxes in the WT and no_WT simulations exhibit small and spatially inhomogeneous differences in the winter and spring seasons even when considered at the grid cell level (Figure 11). Differences in the mean fluxes within individual grid cells are of relatively large magnitude during the summer (Figure 9), but the histogram of mean grid cell differences in the two simulations is symmetric around zero. This indicates that there are compensating grid cells of higher and lower fluxes and therefore little coherent signal of a substantial impact on regional fluxes of heat and moisture. The domain average mean differences in SH in the four seasons (December–February, March–May, June–August, and September–November) are 0.00, 0.04, 0.20, and 0.18 W/m^2. The interquartile range of the grid cell differences in summer and fall are −4.3 to 4.6 and − 2.0 to 2.3 W/m^2, respectively. Domain average seasonal mean differences for LH are 0.00, −0.04, −0.26, and −0.19 W/m^2. Thus, although the action of WT in the model serves to slightly decrease the d02 averaged mean LH flux during summer and fall it increases (by almost equal magnitude) the SH flux. As is the case with T2M and Q2M, bootstrapped confidence intervals on grid cell specific fluxes from the no_WT simulation are generally inclusive of median values from the WT simulation for all grid cells except for SH during summer and for LH in fall (Figure 11), and thus, these differences are not statistically significant.

WT impacts on seasonal mean PBLH are uniformly small when spatially averaged over d02 (Figure 12). The mean impact of WT on PBLH in any grid cell within d02 has a maximum value of +60 m in summer and a minimum value of −60 m (where negative indicates lower PBLH heights in the WT simulation) also in summer. These perturbations are substantial relative to the domain mean PBLH of 780 m, but they are also considerably smaller than the discrepancy between seasonal mean PBLH estimates from the WRF no_WT simulation and those derived from MERRA-2 and NARR (Table 4). As indicated by Figure 12, the spatial patterns of these differences are complex and as indicated by the histograms of PBLH perturbations given in Figure 12, these differences exhibit a Gaussian distribution centered on zero. Accordingly, the spatial mean of the grid cell seasonal mean differences are 0.5, 0.3, −1.8, and 0.8 m for winter to fall (Figure 12). During summer, the mean difference in pairwise samples of grid cell PBLH in the WT and no_WT simulations indicates a slightly larger fraction of grid cells in d02 with lower PBLH in the WT simulation. This is likely due to the manner in which PBLH is diagnosed in the MYNN2.5 scheme (via a TKE method combined with the method based on the increase in potential temperature; Nakanishi & Niino, 2009; Xie et al., 2013).

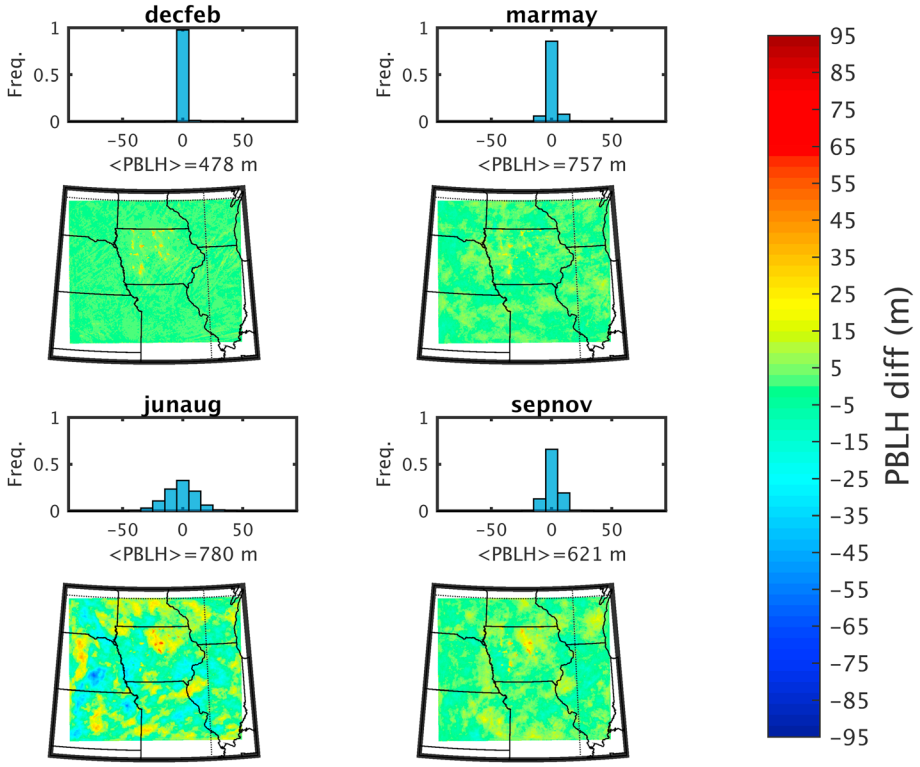

Figure 12. Grid cell differences within d02 in the mean PBLH from the WRF simulation with wind turbines minus the no_WT simulation. Each panel shows a different season (decfeb = winter, marmay = spring, junaug = summer, sepnov = fall). In each panel the histogram denotes the number of grid cells that exhibit a difference of a given magnitude (discretized with a 10 m interval), while the value <PBLH> denotes the mean value in the no_WT simulation during that season. The maps show the spatial patterns within the inner domain (d02). The scales used in each subplot are consistent across all seasons. PBLH = planetary boundary layer height; WRF = Weather Research and Forecasting; WT = wind turbine.

4. Discussion and Concluding Remarks

Decarbonizing the electricity supply via increased use of renewable energy sources has been proposed as an effective climate change mitigation strategy, but concerns have been raised that impacts from large-scale deployments of WTs may cause substantial perturbations to near-surface temperature, humidity, and even precipitation regimes. However, very few assessments have been conducted for climatologically relevant time periods using realistic representations of both the WT locations and their interaction with the atmospheric flow field.

The action of WT to extract momentum from the atmosphere and harness it to generate electrical power inevitably disrupts the flow near to and downwind of the rotor plane. However, our simulations that are predicated on detailed and accurate representations of both the WT themselves and the regional climate of the central United States indicate that the downstream impacts from the 5.2 GW of installed WT capacity within the state of Iowa on near-surface climate variables are smaller than have been reported in previous model analyses (see summary in Table 1). Consistent with a priori expectations and physical arguments, the effects of WT on near-surface climate variables are confined primarily to the near vicinity of WT. For the simulation domain centered on one of the highest densities of onshore WT deployments, the impact of WT operation on local to mesoscale climate is inevitably not zero, but it is demonstrably of modest magnitude. Only in the summertime is the impact of the WT sufficient to cause the median value of Q2M, SH, or LH from more than 5% of grid cells in the WT simulation to lie beyond the bootstrapped 95% confidence interval computed for output from those same grid cells in the no_WT run. Even during this season of maximum WT impact the d02 spatially averaged perturbations (i.e., median of the grid cell median values) of T2M, Q2M, SH, and LH are $< |0.04|$ K, g/kg, W/m^2, and W/m^2, respectively. Individual 4-km by 4-km grid cells, particularly those in which WTs are present, indicate larger effects. For example, during summer, the seasonal mean near-surface air temperature in individual grid cells is up to 0.5 K higher in the WT simulation and specific

humidity is up to 0.4 g/kg higher. There is weak evidence that summertime domain total precipitation may be suppressed by 2.6% in the WT simulation relative to the no_WT simulation, but the impacts on precipitation and the surface fluxes of SH and LH are spatially incoherent and may arise from stochastic effects present in the simulations. While individual grid cells exhibit very large perturbations during summertime SH and LH of up to ±15 W/m^2, the ensemble probability distribution of perturbations from all grid cells are symmetrically distributed about zero. Thus, the spatially aggregated effect is very small. In reporting these values of differences between the no_WT and WT simulation it is also important to note that the magnitude of the effect on the near-surface variables and WSs reported herein may be slightly overestimated due to the negative bias in PBLH during the summer (Table 4). Further, all of the effects on surface fluxes and precipitation reported herein are of smaller magnitude than those that are simulated to have arisen over the study domain due to anthropogenic cropland and pasture expansion and wood harvest within the Great Plains (Chen & Dirmeyer, 2017).

Our results of only modest impact on local to mesoscale climate from the action of WT deployed in the state of Iowa are thus consistent with an analysis of the entire continental WT fleet conducted at coarser spatial resolution over Europe (Vautard et al., 2014). Our results differ from the European study in that it showed statistically significant impacts (of up to ±0.3 K, and 0–5% for precipitation) only during winter, while our simulations indicate statistically significant impacts in the central United States confined to the summer months. This may reflect differences in the base climate of the central United States versus Europe, and/or differences in the spatial resolution of the simulations (≈ 50 km grid resolution in the European study versus 4 km grid resolution in the current study).

Our finding that the impact of WT is maximized in summer is due to the lower WSs during this season within the domain and aerodynamics of the WT rotors. This finding has great relevance for interpreting previous research studies that have considered shorter duration simulations and have focused on summer (Baidya Roy et al., 2004; Miller et al., 2015).

Even though the simulations presented herein are unprecedented in terms of the combination of spatial resolution and duration there are a number of important caveats that must be applied to our results and inferences drawn therefrom. These included, but are not limited to, the following.

1. Our study is naturally dependent on the degree the Fitch parameterization adequately represents the action of WT on the atmosphere. The formulation is based on solid physical basis, and it represents a substantial improvement of approaches applied previously in that it treats the atmospheric drag imposed by WT in a realistic fashion and also the introduction of TKE scales with WS. It has also been subject to independent evaluation. For example, WRF with this WT parameterization was applied to a domain centered on an operating offshore wind farm and was shown to qualitatively reproduce the power deficit at the wind farm scale (Jiménez et al., 2015). Nevertheless, further work is needed to evaluate the ability of WRF-WT simulations to fully represent the impact of WT on near-surface atmospheric properties (Xia et al., 2017). Also, an alternative approach (referred to as the explicit wake parameterization) has been proposed that defines the TKE from random fluctuations around the ensemble average velocity instead of around the grid cell average velocity (Volker et al., 2015). It is possible that adoption of the explicit wake parameterization within our WRF simulations may generate different results for the climate impacts.
2. Our study incorporates simulations over a full calendar year but nevertheless does not represent the full variability of climate over Iowa and the surrounding states. It is possible that due to the action of internal climate modes, the base wind climate in other years may differ (Pryor & Ledolter, 2010; Schoof & Pryor, 2014) sufficiently that the WT climate impacts are amplified or suppressed.
3. Our results are naturally applicable only to the simulation domain studied and to the specific physics packages we employed.
4. We conducted our simulations at so-called convection-permitting resolution. It would be useful to examine the degree to which the climate impacts are dependent on the precise resolution used and also to the lateral boundary conditions employed.
5. The WT installed capacity per square kilometer in Iowa is the highest of any state in the continental United States. Thus, the simulations presented herein reflect impacts from relatively high WT densities. However, the comparatively small domain used herein (approximately 103 to 83°W, 33.5 to 49.5°N) precludes assessment of potential impacts from all WT deployed in the United States on synoptic-scale systems.

Future work should consider to address these caveats and consider the cumulative impacts of WT aggregated over larger spatial areas.

Appendix A: List of Abbreviations

CDF	cumulative density function
CF	capacity factor (power produced relative to installed capacity)
d0X	where *X* is 1 or 2: simulation domain 01 (outer) or 02 (inner)
ENSO	El Niño–Southern Oscillation
ERA	European Reanalysis (i.e., global reanalysis data set produced by European Centre for Medium-Range Weather Forecasts)
FWER	Family-wise error rate
HH	hub height, that is, the height of the nacelle, the center point of the rotor plane of a wind turbine
LH	latent heat
MERRA-2	Modern-Era Retrospective analysis for Research and Applications, version 2
NARR	North American Regional Reanalysis
PBLH	planetary boundary layer height
PPT	precipitation
Q2M	specific humidity at 2-m agl
SH	sensible heat
T2M	air temperature at 2-m agl
TKE	turbulent kinetic energy
USGS	United States Geological Survey
WRF	Weather Research and Forecasting model
WS10	wind speed at 10-m agl
WSHH	wind speed at wind turbine hub height
WS500	wind speed at approximately 500-m agl WT: wind turbine

5. Data Availability

ERA-Interim output is available for download from http://apps.ecmwf.int/datasets/. WT locations as reported by the USGS are available from https://eerscmap.usgs.gov/arcgis/rest/services/wind/wTurbinesWMDyn/MapServer. The NOAA-NCEP real-time global sea surface temperature analyses are available from http://www.nco.ncep.noaa.gov/pmb/products/sst/. Output from NARR is provided by the NOAA/OAR/ESRL PSD, Boulder, Colorado, USA, from their Web site at https://www.esrl.noaa.gov/psd/. Output from MERRA-2 is provided by NASA and is available for download from https://disc.sci.gsfc.nasa.gov/datasets?page=1&keywords=MERRA-2. The WRF model output generated within this project are available for download at http://portal.nersc.gov/archive/home/projects/m2645/www/public_data_iowa/.

Acknowledgments
The U.S. Department of Energy (DE-SC0016438) and Cornell University's Atkinson Center for a Sustainable Future (ACSF-sp2279-2016) funded this research. We thank Adam Brazier and Bennett Wineholt for their assistance in building and maintaining the cloud infrastructure leveraged in this research. This research was enabled by access to a range of computational resources supported by NSF ACI-1541215, those made available via the NSF Extreme Science and Engineering Discovery Environment (XSEDE), program particularly the Jetstream resource (ACI-1548562), and those of the National Energy Research Scientific Computing Center, a DOE Office of Science User Facility supported by the Office of Science of the U.S. Department of Energy under contract DE-AC02-05CH11231. The comments of three reviewers are gratefully acknowledged.

References

Armstrong, A., Burton, R. R., Lee, S. E., Mobbs, S., Ostle, N., Smith, V., et al. (2016). Ground-level climate at a peatland wind farm in Scotland is affected by wind turbine operation. *Environmental Research Letters*, *11*(4). https://doi.org/10.1088/1748-9326/11/4/044024

Baidya Roy, S., Pacala, S. W., & Walko, R. L. (2004). Can large wind farms affect local meteorology? *Journal of Geophysical Research*, *109*, D19101. https://doi.org/10.11029/12004JD004763

Barrie, D. B., & Kirk-Davidoff, D. B. (2010). Weather response to a large wind turbine array. *Atmospheric Chemistry and Physics*, *10*(2), 769–775. https://doi.org/10.5194/acp-10-769-2010

Barthelmie, R. J., Hansen, K. S., & Pryor, S. C. (2013). Meteorological controls on wind turbine wakes. *Proceedings of the IEEE*, *101*(4), 1010–1019. https://doi.org/10.1109/JPROC.2012.2204029

Barthelmie, R. J., & Pryor, S. C. (2014). Potential contribution of wind energy to climate change mitigation. *Nature Climate Change*, *4*(8), 684–688. https://doi.org/10.1038/nclimate2269

Battany, M. C. (2012). Vineyard frost protection with upward-blowing wind machines. *Agricultural and Forest Meteorology*, *157*, 39–48. https://doi.org/10.1016/j.agrformet.2012.01.009

Beljaars, A. (1995). The parametrization of surface fluxes in large-scale models under free convection. *Quarterly Journal of the Royal Meteorological Society*, *121*(522), 255–270. https://doi.org/10.1002/qj.49712152203

Bird, L., Cochran, J., & Wang, X. (2014). *Wind and solar energy curtailment: Experience and practices in the United States, Rep* (p. 58). Colorado: National Renewable Energy Laboratory. Retrieved from https://www.nrel.gov/docs/fy14osti/60983.pdf

Buchard, V., Randles, C. A., da Silva, A. M., Darmenov, A., Colarco, P. R., Govindaraju, R., et al. (2017). The MERRA-2 aerosol reanalysis, 1980 onward. Part II: Evaluation and case studies. *Journal of Climate*, *30*(17), 6851–6872. https://doi.org/10.1175/jcli-d-16-0613.1

Chen, L., & Dirmeyer, P. A. (2017). Impacts of land-use/land-cover change on afternoon precipitation over North America. *Journal of Climate*, *30*(6), 2121–2140. https://doi.org/10.1175/JCLI-D-16-0589.1

Christiansen, M. B., & Hasager, C. B. (2005). Wake effects of large offshore wind farms identified from satellite SAR. *Remote Sensing of Environment*, *98*(2–3), 251–268. https://doi.org/10.1016/j.rse.2005.07.009

Dee, D. P., Uppala, S., Simmons, A., Berrisford, P., Poli, P., Kobayashi, S., et al. (2011). The ERA-Interim reanalysis: Configuration and performance of the data assimilation system. *Quarterly Journal of the Royal Meteorological Society*, *137*(656), 553–597. https://doi.org/10.1002/qj.828

Dudhia, J. (1989). Numerical study of convection observed during the winter monsoon experiment using a mesoscale two-dimensional model. *Journal of the Atmospheric Sciences*, *46*(20), 3077–3107. https://doi.org/10.1175/1520-0469(1989)046%3C3077:NSOCOD%3E2.0.CO;2

Edenhofer, O., Madruga, R. P., Sokona, Y., Seyboth, K., Matschoss, P., Kadner, S., et al. (Eds.) (2012). *Renewable energy sources and climate change mitigation: Special report of the Intergovernmental Panel on Climate Change* (p. 1075). Cambridge, UK: Cambridge University Press.

Ferrier, B. S., Jin, Y., Lin, Y., Black, T., Rogers, E., & DiMego, G. (2002). Implementation of a new grid-scale cloud and precipitation scheme in the NCEP Eta model. In *15th Conf. on Numerical Weather Prediction* (pp. 280–283).

Fitch, A. C. (2015). Climate impacts of large-scale wind farms as parameterized in a global climate model. *Journal of Climate*, *28*(15), 6160–6180. https://doi.org/10.1175/jcli-d-14-00245.1

Fitch, A. C., Olson, J. B., & Lundquist, J. K. (2013). Parameterization of wind farms in climate models. *Journal of Climate*, *26*(17), 6439–6458. https://doi.org/10.1175/jcli-d-12-00376.1

Fitch, A. C., Olson, J. B., Lundquist, J. K., Dudhia, J., Gupta, A. K., Michalakes, J., & Barstad, I. (2012). Local and mesoscale impacts of wind farms as parameterized in a mesoscale NWP model. *Monthly Weather Review*, *140*(9), 3017–3038. https://doi.org/10.1175/mwr-d-11-00352.1

Frandsen, S., Barthelmie, R. J., Jorgensen, H. E., Rathmann, O., Badger, J., Hansen, K., et al. (2009). The making of a second-generation wind farm efficiency model-complex. *Wind Energy*, *12*, 431–444.

Fritsch, J., Kane, R., & Chelius, C. (1986). The contribution of mesoscale convective weather systems to the warm-season precipitation in the United States. *Journal of Climate and Applied Meteorology*, *25*(10), 1333–1345. https://doi.org/10.1175/1520-0450(1986)025%3C1333:TCOMCW%3E2.0.CO;2

Gallus, W. A. Jr., & Bresch, J. F. (2006). Comparison of impacts of WRF dynamic core, physics package, and initial conditions on warm season rainfall forecasts. *Monthly Weather Review*, *134*(9), 2632–2641. https://doi.org/10.1175/MWR3198.1

Gryning, S.-E., Badger, J., Hahmann, A. N., & Batchvarova, E. (2014). Current status and challenges in wind energy assessment. In *Weather matters for energy* (pp. 275–293). Springer. Retrieved from https://www.springer.com/gp/book/9781461492207

Harris, R. A., Zhou, L., & Xia, G. (2014). Satellite observations of wind farm impacts on nocturnal land surface temperature in Iowa. *Remote Sensing*, *6*(12), 12,234–12,246. https://doi.org/10.3390/rs61212234

Jiménez, P. A., Navarro, J., Palomares, A. M., & Dudhia, J. (2015). Mesoscale modeling of offshore wind turbine wakes at the wind farm resolving scale: A composite-based analysis with the weather research and forecasting model over Horns Rev. *Wind Energy*, *18*(3), 559–566. https://doi.org/10.1002/we.1708

Kain, J. S. (2004). The Kain–Fritsch convective parameterization: An update. *Journal of Applied Meteorology*, *43*(1), 170–181. https://doi.org/10.1175/1520-0450(2004)043%3C0170:TKCPAU%3E2.0.CO;2

Keith, D. W., DeCarolis, J. F., Denkenberger, D. C., Lenschow, D. H., Malyshev, S. L., Pacala, S., & Rasch, P. J. (2004). The influence of large-scale wind power on global climate. *Proceedings of the National Academy of Sciences of the United States of America*, *101*(46), 16,115–16,120. https://doi.org/10.1073/pnas.0406930101

LeMone, M. A., Chen, F., Alfieri, J. G., Tewari, M., Geerts, B., Miao, Q., et al. (2007). Influence of land cover and soil moisture on the horizontal distribution of sensible and latent heat fluxes in southeast Kansas during IHOP_2002 and CASES-97. *Journal of Hydrometeorology*, *8*(1), 68–87. https://doi.org/10.1175/JHM554.1

Manwell, J. F., McGowan, J., & Rogers, A. L. (2002). *Wind energy explained: Theory, design and application* (p. 590). Chichester, UK: John Wiley and Sons. https://doi.org/10.1002/0470846127

McCabe, G. J., Palecki, M. A., & Betancourt, J. L. (2004). Pacific and Atlantic Ocean influences on multidecadal drought frequency in the United States. *Proceedings of the National Academy of Sciences of the United States of America*, *101*(12), 4136–4141. https://doi.org/10.1073/pnas.0306738101

Mesinger, F., DiMego, G., Kalnay, E., Mitchell, K., Shafran, P. C., Ebisuzaki, W., et al. (2006). North American regional reanalysis. *Bulletin of the American Meteorological Society*, *87*(3), 343–360. https://doi.org/10.1175/BAMS-87-3-343

Miller, L. M., Brunsell, N. A., Mechem, D. B., Gans, F., Monaghan, A. J., Vautard, R., et al. (2015). Two methods for estimating limits to large-scale wind power generation. *Proceedings of the National Academy of Sciences of the United States of America*, *112*(36), 11,169–11,174. https://doi.org/10.1073/pnas.1408251112

Mlawer, E. J., Taubman, S. J., Brown, P. D., Iacono, M. J., & Clough, S. A. (1997). Radiative transfer for inhomogeneous atmospheres: RRTM, a validated correlated-k model for the longwave. *Journal of Geophysical Research*, *102*(D14), 16,663–16,682. https://doi.org/10.1029/97JD00237

Molod, A., Takacs, L., Suarez, M., & Bacmeister, J. (2015). Development of the GEOS-5 atmospheric general circulation model: Evolution from MERRA to MERRA2. *Geoscientific Model Development*, *8*(5), 1339–1356. https://doi.org/10.5194/gmd-8-1339-2015

Motta, M., Barthelmie, R. J., & Vølund, P. (2005). The influence of non-logarithmic wind speed profiles on potential power output at Danish offshore sites. *Wind Energy*, *8*(2), 219–236. https://doi.org/10.1002/we.146

Nakanishi, M., & Niino, H. (2006). An improved Mellor–Yamada level-3 model: Its numerical stability and application to a regional prediction of advection fog. *Boundary-Layer Meteorology*, *119*(2), 397–407. https://doi.org/10.1007/s10546-005-9030-8

Nakanishi, M., & Niino, H. (2009). Development of an improved turbulence closure model for the atmospheric boundary layer. *Journal of the Meteorological Society of Japan. Ser. II*, *87*(5), 895–912.

National Renewable Energy Laboratory (2008). 20% wind energy by 2030, DOE/GO-102008-102567. (102248 pp.). NREL. Retrieved from http://www.nrel.gov/docs/fy08osti/41869.pdf

Peña, A., Gryning, S. E., & Hahmann, A. N. (2013). Observations of the atmospheric boundary layer height under marine upstream flow conditions at a coastal site. *Journal of Geophysical Research: Atmospheres*, *118*, 1924–1940. https://doi.org/10.1002/jgrd.50175

Peterson, T. C., & Baringer, M. (2009). State of the climate in 2008. *Bulletin of the American Meteorological Society*, *90*(8), S1–S196. https://doi.org/10.1175/BAMS-90-8-StateoftheClimate

Powers, J. G., Klemp, J. B., Skamarock, W. C., Davis, C. A., Dudhia, J., Gill, D. O., et al. (2017). The weather research and forecasting (WRF) model: Overview, system efforts, and future directions. *Bulletin of the American Meteorological Society*, *98*(8), 1717–1737. https://doi.org/10.1175/BAMS-D-15-00308.1

Prein, A. F., Langhans, W., Fosser, G., Ferrone, A., Ban, N., Goergen, K., et al. (2015). A review on regional convection-permitting climate modeling: Demonstrations, prospects, and challenges. *Reviews of Geophysics*, *53*(2), 323–361. https://doi.org/10.1002/2014RG000475

Prospathopoulos, J. M., Politis, E. S., Rados, K. G., & Chaviaropoulos, P. K. (2011). Evaluation of the effects of turbulence model enhancements on wind turbine wake predictions. *Wind Energy*, *14*(2), 285–300. https://doi.org/10.1002/we.419

Pryor, S. C., & Barthelmie, R. J. (2002). Comparison of potential power production at on- and off- shore sites. *Wind Energy*, *2001*(4), 173–181.

Pryor, S. C., Barthelmie, R. J., Young, D. T., Takle, E. S., Arritt, R. W., Flory, D., et al. (2009). Wind speed trends over the contiguous United States. *Journal of Geophysical Research*, *114*, D14105. https://doi.org/10.1029/2008JD011416

Pryor, S. C., & Ledolter, J. (2010). Addendum to: Wind speed trends over the contiguous USA. *Journal of Geophysical Research*, *115*, D10103. https://doi.org/10.1029/2009JD013281

Quarton, D., & Ainslie, J. (1990). Turbulence in wind turbine wakes. *Wind Engineering*, *14*(1), 15–23.

Rajewski, D. A., Takle, E. S., Prueger, J. H., & Doorenbos, R. K. (2016). Toward understanding the physical link between turbines and micro-climate impacts from in situ measurements in a large wind farm. *Journal of Geophysical Research: Atmospheres*, *121*, 13,392–13,414. https://doi.org/10.1002/2016JD025297

Randles, C. A., da Silva, A. M., Buchard, V., Colarco, P. R., Darmenov, A., Govindaraju, R., et al. (2017). The MERRA-2 aerosol reanalysis, 1980 onward. Part I: System description and data assimilation evaluation. *Journal of Climate*, *30*(17), 6823–6850. https://doi.org/10.1175/jcli-d-16-0609.1

Reichle, R. H., Liu, Q., Koster, R. D., Draper, C. S., Mahanama, S. P., & Partyka, G. S. (2017). Land surface precipitation in MERRA-2. *Journal of Climate*, *30*(5), 1643–1664. https://doi.org/10.1175/JCLI-D-16-0570.1

Reynolds, R. W., & Chelton, D. B. (2010). Comparisons of daily sea surface temperature analyses for 2007–08. *Journal of Climate*, *23*(13), 3545–3562. https://doi.org/10.1175/2010JCLI3294.1

Schmid, P., & Niyogi, D. (2012). A method for estimating planetary boundary layer heights and its application over the ARM Southern Great Plains site. *Journal of Atmospheric and Oceanic Technology*, *29*(3), 316–322. https://doi.org/10.1175/JTECH-D-11-00118.1

Schoof, J. T., & Pryor, S. C. (2014). Assessing the fidelity of AOGCM-simulated relationships between large-scale modes of climate variability and wind speeds. *Journal of Geophysical Research: Atmospheres*, *119*, 9719–9734. https://doi.org/10.1002/2014JD021601

Skamarock, W. C., Klemp, J. B., Dudhia, J., Gill, D. O., Barker, D. M., Wang, W., & Powers, J. G. (2005). *A description of the advanced research WRF version 2. Rep* (p. 88). Boulder, CO: NCAR tech. Note NCAR/TN-468+STR.

Smith, C. M., Barthelmie, R. J., & Pryor, S. C. (2013). In situ observations of the influence of a large onshore wind farm on near-surface temperature, turbulence intensity and wind speed profiles. *Environmental Research Letters*, *8*(3), 034006. https://doi.org/10.1088/1748-9326/8/3/034006

Smith, J. A., Baeck, M. L., Villarini, G., Wright, D. B., & Krajewski, W. (2013). Extreme flood response: The June 2008 flooding in Iowa. *Journal of Hydrometeorology*, *14*(6), 1810–1825. https://doi.org/10.1175/JHM-D-12-0191.1

Sun, J., Xue, M., Wilson, J. W., Zawadzki, I., Ballard, S. P., Onvlee-Hooimeyer, J., et al. (2014). Use of NWP for nowcasting convective precipitation: Recent progress and challenges. *Bulletin of the American Meteorological Society*, *95*(3), 409–426. https://doi.org/10.1175/BAMS-D-11-00263.1

Tewari, M., Chen, F., Wang, W., Dudhia, J., LeMone, M., Mitchell, K., et al. (2004). Implementation and verification of the unified NOAH land surface model in the WRF model. In *20th Conference on Weather Analysis and Forecasting/16th Conference on Numerical Weather Prediction* (1115, 6 pp.).

Vautard, R., Thais, F., Tobin, I., Breon, F. M., Devezaux de Lavergne, J. G., Colette, A., et al. (2014). Regional climate model simulations indicate limited climatic impacts by operational and planned European wind farms. *Nature Communications*, *5*, 3196. https://doi.org/10.1038/ncomms4196

Volker, P. J. H., Badger, J., Hahmann, A. N., & Ott, S. (2015). The Explicit Wake Parametrisation V1.0: A wind farm parametrisation in the mesoscale model WRF. *Geoscientific Model Development*, *8*, 3481–3522. https://doi.org/10.5194/gmdd-3488-3481-2015

Volker, P. J. H., Hahmann, A. N., Badger, J., & Jørgensen, H. E. (2017). Prospects for generating electricity by large onshore and offshore wind farms. *Environmental Research Letters*, *12*(3), 034022. https://doi.org/10.1088/1748-9326/aa5d86

Wang, C., & Prinn, R. G. (2010). Potential climatic impacts and reliability of very large-scale wind farms. *Atmospheric Chemistry and Physics*, *10*(4), 2053–2061. https://doi.org/10.5194/acp-10-2053-2010

Wilks, D. S. (2011). *Statistical methods in the atmospheric sciences*. Oxford, UK: Academic Press.

Wiser, R., & Bolinger, M. (2016). 2015 wind technologies market report (Rep., 102 pp.). US Department of Energy: Office of Scientific and Technical Information. Retrieved from https://energy.gov/sites/prod/files/2016/08/f33/2015-Wind-Technologies-Market-Report-08162016.pdf

Wiser, R., & Bolinger, M. (2017). 2016 wind technologies market report (Rep., 94 pp.). U.S. Department of Energy: Office of Energy Efficiency and Renewable Energy, Report available from SciTech Connect http://www.osti.gov/scitech

Wiser, R., Jenni, K., Seel, J., Baker, E., Hand, M., Lantz, E., & Smith, A. (2016). Expert elicitation survey on future wind energy costs. *Nature Energy*, *1*(10), 16135. https://doi.org/10.1038/nenergy.2016.135

Xia, G., Cervarich, M. C., Roy, S. B., Zhou, L., Minder, J. R., Jimenez, P. A., & Freedman, J. M. (2017). Simulating impacts of real-world wind farms on land surface temperature using the WRF model: Validation with observations. *Monthly Weather Review*, *145*(12), 4813–4836. https://doi.org/10.1175/MWR-D-16-0401.1

Xie, B., Fung, J. C. H., Chan, A., & Lau, A. (2012). Evaluation of nonlocal and local planetary boundary layer schemes in the WRF model. *Journal of Geophysical Research*, *117*, D12103. https://doi.org/10.1029/2011JD017080

Xie, B., Hunt, J. C., Carruthers, D. J., Fung, J. C. H., & Barlow, J. F. (2013). Structure of the planetary boundary layer over southeast England: Modeling and measurements. *Journal of Geophysical Research: Atmospheres*, *118*, 7799–7818. https://doi.org/10.1002/jgrd.50621

Zhang, W., Markfort, C. D., & Porté-Agel, F. (2013). Experimental study of the impact of large-scale wind farms on land–atmosphere exchanges. *Environmental Research Letters*, *8*(1), 015002. https://doi.org/10.1088/1748-9326/8/1/015002

Zhou, L., Tian, Y., Baidya Roy, S., Thorncroft, C., Bosart, L. F., & Hu, Y. (2012). Impacts of wind farms on land surface temperature. *Nature Climate Change*, *2*(7), 539–543.